

An assessment of the reproducibility of the Gemini retro focusing system

Contact david.carroll@strath.ac.uk

D.C. Carroll, M. Coury, G. Scott*, P. McKenna

Department of physics, University of Strathclyde, SUPA, Glasgow G4 0NG, UK

M.J.V. Streeter, H. Nakamura, Z. Najmudin

Physics Department, Imperial College London, London, SW7 2AZ, UK

F. Fiorini, S. Green

School of Physics and Astronomy, University of Birmingham, Birmingham B15 2TT, UK

J.S. Green, P. Foster, R. Heathcote, K. Poder, D. Symes, R.J. Clarke, R. Pattathil, D. Neely

*Central Laser Facility, STFC RAL, Oxfordshire OX11 0QX, UK

Introduction

In the Astra-Gemini target chamber solid targets are positioned relative to the tight focus of the laser for an F/2 off-axis parabolic mirror (OAP) using a retro-focusing system. This system uses the focusing OAP itself to collect back-scattered light from the target and sends it back along the beam path. A leak of this light is taken through a mirror and focused down onto a camera. The camera is positioned relative to the focusing lens such that the backscattered light is at tight focus on the camera at the point where the target is at the tight focus position of the OAP.

In this report we present results from a test of the retro-focusing system. The test looked at the repeatability of bringing a target to focus with the system by a single user. We also compared repeatability across multiple users. This is important as positioning the target consistently in relation to the laser focus is essential for solid target experiments.

Astra-Gemini Retro-focus system

The retro focusing system for Astra-Gemini, see figure 1, uses a green (532 nm) laser injected through the back of a high reflectivity dielectric infra-red mirror which is matched to the main laser. The retro system images the green light back scattered from the target. The green laser is used to maximise light collected on camera (using infra-red would result in a much weaker signal through a high reflectivity dielectric infra-red mirror) and the shorter wavelength means a tighter diffraction limited focal spot. This in turn means, if the system is fully optimised, that the green laser will focus and defocus faster than the infra-red laser light and so make it potentially easier for operators to bring targets to focus.

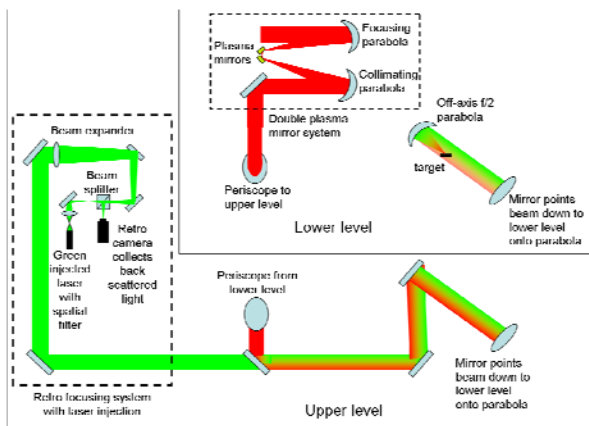


Fig 1: Astra Gemini Beam path with Retro system layout. It also shows how the beam path is split between an upper and a lower level in the chamber.

Retro-focus system test procedure

A solid target with a flat surface, see figure 2, is used for the test, the target is the flat side of a 3 mm diameter Al stalk. The

target is mounted on a three-dimensional motorised stage (dc motors) with magniscales that record the position of the target. The incident angle of the laser, focused with an F/2 OAP, onto target is 35 degrees.

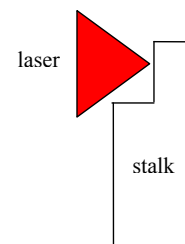


Fig 1: target stalk that was retro focused with.

Five operators of various levels of experience in conducting experiments at the Central Laser Facility were asked to bring the target to the tight focus position of the laser five times in a row. Each operator looked at the retro focus system monitor and attempted to bring it to best focus (minimised spot size as they judged it) by moving the target along its z-axis, which is set by eye to be parallel to the focusing axis of the parabolic mirror. When the operator believed the target to be at tight focus the position value on the magniscale was recorded.

Results

The results of different operators' multiple attempts to bring the target to tight focus are presented in table 1. The operators combined mean position was 1008.5 μm with a standard deviation of 15.5 μm . The full range of values within this is 57 μm (27.5 μm below mean and 29.5 μm above mean). For the purpose of this report the mean position of all operators attempts at bringing the target to tight focus is assumed to be the tight focus position.

The size of the focal spot of the laser in infra-red has previously been measured to be $\sim 2.5 \mu\text{m}$ diameter (d_0 , FWHM) [1]. The focal spot distribution is closer to a super Gaussian than a Gaussian, this means that the radius at $1/e^2$ (otherwise known as the beam waist, w_0) has the following relation to the FWHM: $w_0 = 0.65d_0$. The beam waist is important as it enables us to calculate the Rayleigh range, z_R , of the Astra-Gemini laser with an F/2 parabola:

$$z_R = \frac{\pi w_0^2}{\lambda}$$

Where λ is the laser wavelength, this is 800 nm for the Astra-Gemini laser. The Rayleigh range is 10.4 μm . Note that if the beam spot was a Gaussian distribution then $z_R = 17.7 \mu\text{m}$.

The standard deviation of the mean tight focus position for all operators (15.5 μm) is $\sim 50\%$ greater than the Rayleigh range for a super Gaussian spot (10.4 μm). Only one operator had their

standard deviation just within the Rayleigh range but even then the difference between their lowest and maximum value positions was double the Rayleigh range.

operator	position z (mm)	Mean (mm)	standard deviation	Min (mm)	Max (mm)	Max-Min (mm)
1	1.003	1.0028	0.014618	0.981	1.022	0.041
5 years experience	1.022					
	1.006					
	0.981					
	1.002					
2	1.025	1.018	0.015411	1.001	1.038	0.037
less than 1 year experience	1.004					
	1.038					
	1.001					
	1.022					
3	1.007	1.00800	0.011726	0.99	1.019	0.029
less than 1 year experience	0.99					
	1.019					
	1.018					
	1.006					
4	1.007	0.996	0.008093	0.986	1.007	0.021
5 years experience	0.986					
	0.996					
	1					
	0.991					
5	0.988	1.0178	0.018377	0.988	1.034	0.046
1 year experience	1.013					
	1.029					
	1.025					
	1.034					
Combined values		1.00852	0.015541	0.981	1.038	0.057

Tab. 1: The motor positions for five attempts at getting the target at tight focus for five different operators are listed. The average value for each operator and the overall average are listed along with the standard deviation, the minimum and maximum position values and the difference between these.

When looking at individual operators multiple attempts at focusing there was no trend (limited over 5 attempts) of later attempts getting closer together. If operators got use to retro focusing and became more consistent we would expect later attempts to be closer together.

operator	Mean (mm)	difference between operator mean and overall mean (μm)
1	1.0028	-5.72
2	1.018	9.48
3	1.00800	-0.52
4	0.996	-12.52
5	1.0178	9.28
overall	1.00852	

Tab. 2: The average positions for the five operators and the differences between these values and the overall average.

If we look at individual operators average positions compared to the overall average position for all operators, we find that only one operator (admittedly the most self consistent) was just outside the Rayleigh range when comparing the differences between the individual averages to the overall group average,

see table 2. This is considerably more consistent compared to the standard deviation of the individual attempts.

Conclusions

The retro-focusing system in the Astra-Gemini target area was tested for reproducibility for operators and across multiple operators.

We recommend that with the current retro-focusing system, when bringing the target to best focus an average of multiple positions should be taken. It was found that all operators were either within or very close to the Rayleigh range when comparing individual averages to the overall average position.

This is especially important as the current trend for experiments on Astra-Gemini is the use of multiple shifts to maximise the utilisation of laser time. This means that there is a greater reliance on consistency of target alignment across multiple operators.

Relying on getting close to best focus with a single attempt, even after multiple attempts, is not recommended as only one operator was consistent enough to have a standard deviation within the Rayleigh range and one other operator with a standard deviation close to the Rayleigh range. Even for these operators the differences between minimum and maximum positions was much greater than the Rayleigh range.

There are several ongoing projects to improve the positioning of the target relative to focus currently being investigated for Gemini. These include adding a wavefront sensor to the current retro-focusing system which will enable the focusing parameter of the wavefront to be used to aid target positioning. Another project is the development of a modified interferometric target positioning system as an alternative to the retro-focusing system, this has the potential for sub-micron accuracy.

References

1. D.C. Carroll *et al*, New Journal of Physics **12** 045020 (2010)

Coherent control of high harmonic generation from relativistically oscillating plasmas via elliptically polarized laser pulses

Contact b.dromey@qub.ac.uk

B. Dromey, M. Zepf, M. Yeung, T. Dzelzainis

*Department of Physics and Astronomy
Queens University Belfast, University Road, BT7 1NN*

D. Kiefer, J. Schreiber

Max Planck Institute of Quantum Optics, Garching, Munich

F. Quere

Groupe de Physique à Haute Intensité, CEA Saclay, Gif-sur-Yvette, France

R. Marjoribanks

Department of Physics, University of Toronto, Canada;

Introduction

The relativistically oscillating plasma medium has been proven to provide a robust mechanism for the generation of bright beams of extreme ultraviolet (XUV) [1] and X-ray [2] harmonic radiation, with clear evidence attosecond phase locking in reflection[3]. However, under certain experimental conditions, generating HHG in transmission from ultrathin foils [4] may prove a more attractive geometry. For the first time coherent control of harmonic generation is performed using the Gemini laser system. This is achieved by varying the ellipticity of the generating laser pulses to switch on and off the generation mechanism for harmonic beams generated in transmission from ultrathin (nm scale) foils. This represents a key development in the proof of principle for polarisation gating of relativistic plasma oscillations for single intense attosecond pulse generation. Significantly, for the first time, fundamental predictions from simulations and analytic theory for harmonic generation from relativistically oscillating plasmas are examined experimentally in the context of a near 1-D interaction.

High harmonic generation from relativistically oscillating plasmas – reflection and transmission

When a laser pulse is incident on a solid density surface the leading edge of the pulse rapidly ionises the target via avalanche ionization creating an overdense plasma (with respect to the incident radiation). Under high contrast laser conditions ($>10^9$ of peak intensity at ~ 1 -2ps before the main pulse) the plasma that is formed has a short scale length and becomes an efficient reflecting surface which couples to the oscillating electric field of the driving laser pulse. In essence this critical density plasma constitutes a relativistic mirror-like surface from which the incident radiation is reflected and subsequently up-shifted in an oscillatory extension to Einstein's relativistic Doppler effect. The theory of this oscillatory extension is described in the theory of relativistic spikes by Baeva et al [5].

It is important to remember, however, that this is a macroscopic picture of the microscopic physics that is at the core of the harmonic generation mechanism – coherently driven electron oscillations. While harmonic emission in the specularly reflected direction from bulk solid density targets is generally well understood it has recently become clear that in the limit of few nm foils the relativistically oscillating mirror approximation does not represent the full picture. The strongly driven electron oscillations not only emit in the specular direction [1] but also in the laser forward, or transmitted direction [4].

The exciting possibility of coherently controlling beams of harmonic radiation from ultrathin foils in transmission is examined here for the first time.

Experimental setup

To investigate the transmission of harmonics from ultrathin foils the contrast enhancing double plasma mirror setup on the North Beam of the Astra Gemini laser was used to increase the near time laser contrast to $\sim 10^9$ at ~ 3 ps before the arrival of the main pulse. The cleaned pulse, with ~ 7 J in ~ 50 fs, was focused using an F/3 off axis parabola to a $\sim 3\mu\text{m}$ full width half maximum focal spot containing $>50\%$ of the incident energy. This resulted in an interaction intensity of $2.5 \pm 1 \times 10^{20} \text{Wcm}^{-2}$. The target was 200nm C placed normal to the incident beam implying an *s*-polarised interaction. The ellipticity of the incident radiation was varied using a $\frac{1}{4} \lambda$ waveplate.

For this experiment a custom built diagnostic with the ability to simultaneously diagnose electron, ion and XUV spectra on a single shot was used. A schematic of the instrument is shown in figure 1. The key benefit of such a spectrometer design is that all aspects (in transmission at least) of the interaction can be examined on a single shot basis.

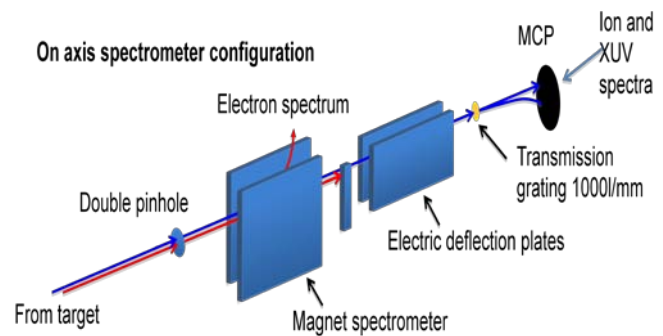


Figure 1 Single shot XUV, electron and ion spectra detection. The double pinhole setup at the entrance allowed a narrow beam to be collected for high spectral resolution for ion and XUV spectra while a wider pinhole was used to collect the electron spectra.

Results

Figure 2 shows a typical image from the MCP detector (Figure 1) recorded for a 200nm C target interaction with linearly polarized light. The saturated vertical feature is an ion spectrum with the Thompson parabola voltage turned off. The XUV spectrum from the transmission grating lies along the 45 deg line (labeled). As can be seen clearly the XUV spectrum under these conditions is dominated by harmonic emission. A lineout of this spectrum (Figure 3, black trace) shows the harmonic orders span the wavelength range $\sim 115\text{nm}$ (7^{th}) to $<8\text{nm}$ ($>100^{\text{th}}$).

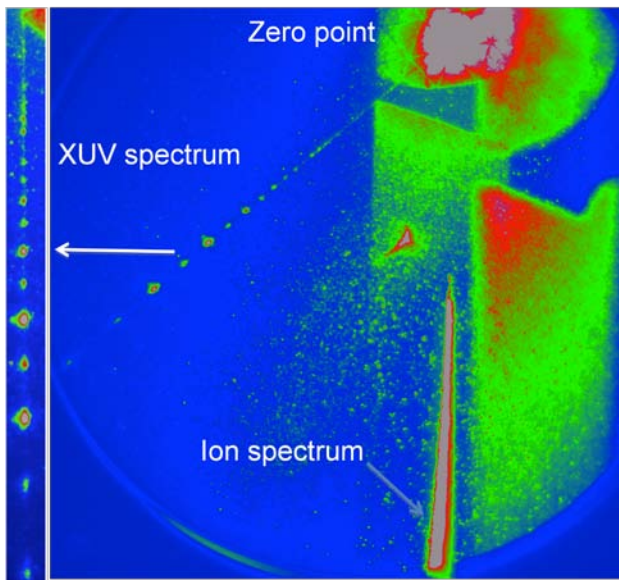


Figure 2 Typical ion and X-ray spectra recorded on the MCP detector at the end of the detector. In this shot the voltage on the Thompson parabola plates is reduced for clarity of the XUV spectrum.

A key feature of this spectrum is the very clear odd-even asymmetry of the harmonic orders. This asymmetry is due to the interaction geometry. Since the target is placed normal to the incident laser pulse the polarisation is predominantly s . As a result there is no strong component of the E-field of the incident laser pulse perpendicular to the plasma surface to drive an oscillation at ω_0 (the laser frequency). Instead the oscillation of the surface is driven by the $\mathbf{v} \times \mathbf{B}$ force at $2\omega_0$. Since the harmonic generation process is therefore largely driven twice per cycle only odd orders can constructively interfere, resulting in a spectrum dominated by odd order harmonics. This is a direct observation of the selection rules for harmonics from relativistically oscillating plasmas given by Lichters[6].

However, Figure 3 also shows that there is some even order contribution to the harmonic spectrum. Initial analysis indicates that this is due to a deviation from a pure 1-D interaction due to denting of the target surface via the ponderomotive force of the laser. This dent creates a p -polarised component of the interaction allowing the plasma to be driven by the electric field of the laser at ω_0 and hence generate even orders, albeit at a significantly reduced efficiency.

Coherent control of relativistically oscillating plasmas

Another prediction of the Lichters selection rules is that high harmonic generation will be suppressed for circularly polarized light. This is due to the fact that the oscillatory components of the driving laser are absent for circular polarization – hence coherent oscillations of the plasma are inhibited. To investigate this the polarization of the Gemini North Beam was changed from linear to circular by the use of a $\frac{1}{4} \lambda$ waveplate. The resulting spectrum is shown in Figure 3, red trace.

As can be seen there is a significant reduction in harmonic yield (>100 for some orders) under circularly polarized conditions. It appears that, although unresolved, there may be a significant harmonic contribution to the signal above 100^{th} order for linear polarisation which is suppressed when using circularly polarized light. This important observation indicates that it will be possible to coherently control, under the correct conditions, harmonic generation extending to 100 's of eV. It is anticipated that this will permit the use of polarization gating [6] techniques to generate isolated attosecond pulses in the keV spectral range [2].

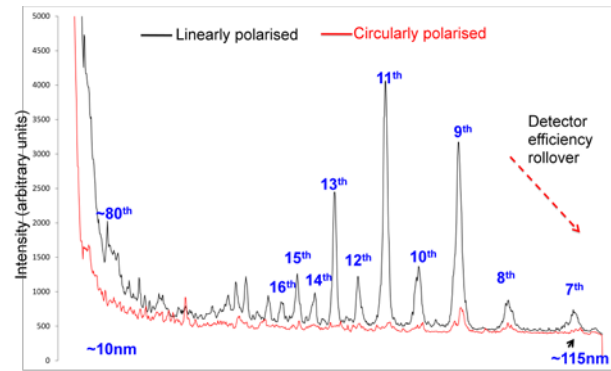


Figure 3 Coherent control of high harmonic generation from relativistically oscillating plasma surfaces in transmission from thin foils. The black trace shows strong harmonic emission for linear polarisation while the signal is strongly suppressed for circular polarization.

Conclusions

The first observation of high harmonic generation for relativistically oscillating plasma surfaces in transmission from thin foils has been performed on the Gemini laser system. Unambiguous odd-even asymmetry has been observed in the harmonic spectrum indicating the preservation of near 1-D interaction conditions. This has permitted the first experiment to be performed that clearly shows that relativistic plasma oscillations can be coherently controlled by varying the ellipticity of the driving laser in the absence of other geometrical constraints (such as oblique incidence etc). This important advance is the first indication that polarization gating by using mixed polarization states [6] (i.e. elliptical-instantaneously linear-elliptical) will be possible, opening the door to intense single attosecond pulse generation for the first time.

Acknowledgements

The authors would like to acknowledge the dedicated support of the Gemini laser staff and the CLF technical support.

References

1. Dromey B. *et al*, Nat. Phys. **2**, 456 - 152 (2006)
2. Dromey B. *et al*, Phys. Rev. Lett. **99**, 085001 (2007)
3. Nomura Y. *et al* Nat. Phys. **5**, 124 - 128 (2009)
4. George, H *et al* New J. Phys. **11** 113028 (2009)
5. Baeva T. *et al*., Phys. Rev. E, **74**, 046404 (2006)
6. Rykovanov S.G. *et al*, New J. Phys. 10 No 2 (2008)

TLD measurements of electron and X-ray emission from different materials irradiated by the Gemini laser.

Contact fxf817@bham.ac.uk

F. Fiorini

School of Physics and Astronomy, University of Birmingham,
Birmingham B15 2TT, UK

S. Green

Hall Edwards Radiotherapy Research Group, University Hospital
Birmingham NHS Trust, Birmingham B15 2TH, UK

J.S. Green, R.J. Clarke, R. Heathcote, D. Symes, K. Poder, R. Pattathil, D. Neely

Central Laser Facility, STFC RAL, Oxfordshire OX11 0QX, UK

D.C. Carroll, M. Coury, G. Scott, P. McKenna

Department of physics, University of Strathclyde, SUPA,
Glasgow G4 0NG, UK

M.J.V. Streeter, Z.Najmudin

Physics Department, Imperial College London, London,
SW7 2AZ, UK

Introduction

We present the experimental results from the radiological commissioning of the Astra Gemini laser upon installation of a new tight-focusing off-axis parabola (F/2 OAP) in the laser system.

During the interaction of the intense laser pulse with a target, a large part of the laser energy is converted into a population of hot electrons. The electron population is created on the target surface irradiated by the laser, with a spectrum believed to follow a Maxwellian distribution and moving inside the target they create a strong electric field (up to the order of TV/m). Given the very high current, their propagation requires a balancing return current from the background plasma. Upon reaching the rear surface of the target some of the hottest electrons escape, but most of them are attracted back into the target. A similar situation later occurs at the front of the target: most of the electrons return to the front surface and some escape. This phenomenon is called electron refluxing [1]. The percentage of refluxing electrons and the number of refluxes change with the target and laser beam characteristics [2, 3]. During its multiple paths inside the target, the electron beam emits X-rays, strictly dependent on target and laser properties.

With this preliminary experiment we aimed to measure the dose due to the emitted photons and electrons and to characterise separately the two beams. These data will also lead to greater understandings of the reflux process.

Experimental set-up

In the experiment we used Thermo Luminescent Dosimeter (TLD-700) chips to record the dose carried by electrons and photons produced by the interaction the Gemini laser and solid targets. The TLD-700 chips used consisted of LiF: Mg, Ti. Their size was (3.2 x 3.2 x 0.89) mm, and they were inserted between absorbers to form a stack.

When ionising radiation interacts with the TLD crystals, the radiation deposits either all or part of the initial energy in the material. Some of the atoms in the material absorb that energy, producing free electrons and holes. The imperfections in the crystal lattice, due to Mg and Ti impurities, act as sites where free electrons can become trapped, locking them in the crystal. Heating the crystal causes the release of those trapped electrons and their return into the original ground state releasing the acquired energy as light. This light is then detected and the number of optical photons counted is proportional to the amount of initial energy deposited in the crystal. It follows that TLD chips can be read only once, but they can be reused many times after being annealed in order to remove any remnant signal. Their sensitivity is slightly dependent on the energy of

the ionising particles as shown in [4], but above 150 keV the efficiency is seen to approach 1.0. The minimum photon energy that can be detected is approximately 30 keV. The TLDs were calibrated using Co⁶⁰ gamma rays, and was traceable to the appropriate UK Primary Standard.

In the Astra Gemini target chamber the TLD stacks were positioned around the target as shown in Fig.1 (a), (b). Each stack was composed of an alternating arrangement of TLD chips and filters made of aluminium and stainless steel (object on the bottom of the Fig.1 (c)). The nine inner ring stacks contained three TLD chips each and covered an angular range between -124 and 60 degrees (where 0 deg. is the laser direction), the five outer ring stacks instead contained six TLD chips and covered an angular range between -30 and 50 degrees. In the majority of cases each outer ring stack had on its front a dipole magnet (object on the top in Fig.1 (c)) to deviate the electrons and therefore measure only the dose due to the photons emitted by the target. Two stacks of the outer ring were placed under the laser axis (~ 5 degrees). The inner and outer stack rings were placed at distances of 20 cm and 45 cm, respectively, from the centre of the target.

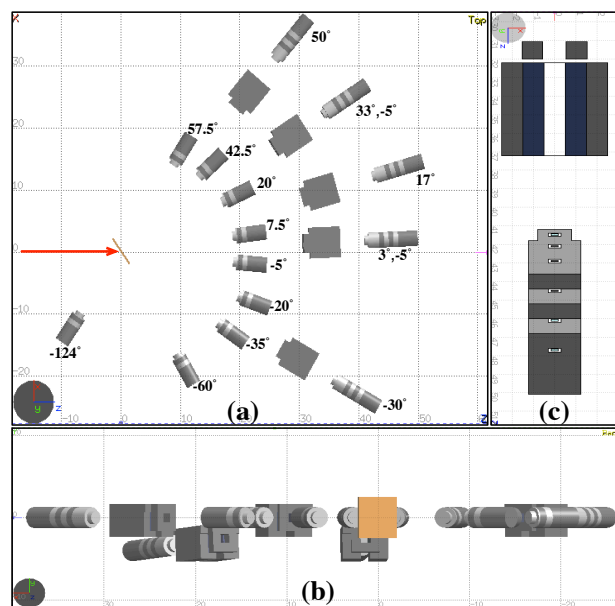


Fig.1 Experimental set-up showing the stack disposition around the target: (a) on ZX plane and (b) on XY plane. (c) Stack of the outer ring showing the magnet on the top and the sequence of absorbers and TLD chips on the bottom.

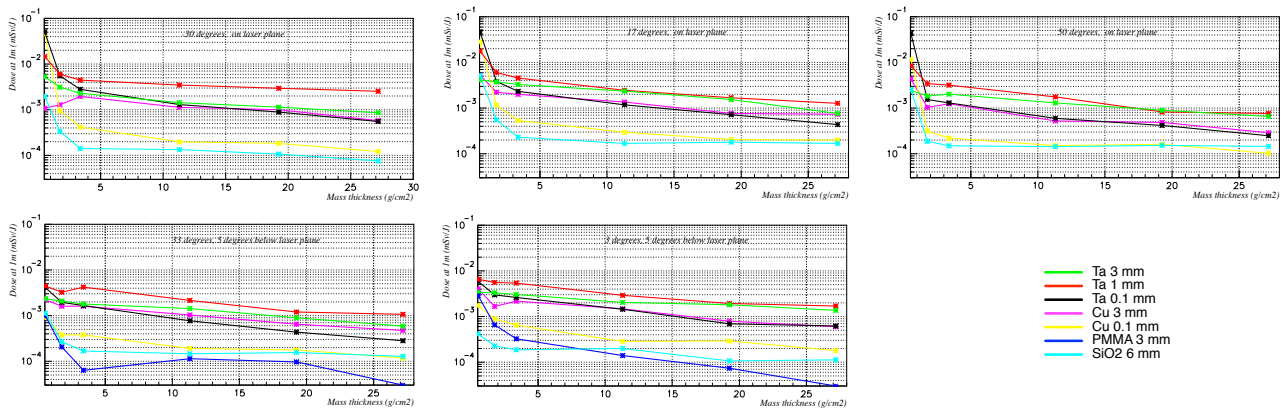


Fig.2 Dose measured from the TLD chips of the outer ring as a function of the mass thickness along the stack. The dose due to the only produced X-rays is shown to be similar if measured from the TLDs of the stacks placed on the laser plane (on the left) and almost always lower if measured from the TLD stacks placed 5 degrees below the laser plane (on the right), particularly for the first TLD chips.

Targets made of different materials and with different thicknesses were irradiated: Ta (0.1 mm, 1 mm and 3 mm), Cu (0.1 mm and 3 mm), PMMA (3 mm) and SiO₂ (6 mm). This wide selection was used to find out which material and which thickness maximised the number of produced X-rays and/or electrons noticeable from the dose absorbed by the TLDs.

In order to achieve good signal to noise levels, we fired multiple shots under identical conditions until the accumulated laser energy on each target was ~150 J. As we conducted the measurements at high contrast, the average deposited energy per shot was (4.5 ± 0.7) J. The diameter of the focal spot of the laser was measured to be ~2.5 μm and the duration of the pulse ~60 fs: the laser intensity was 8×10^{20} Wcm^{-2} . The incident angle of the laser on target, focused with an F/2 OAP, was 35 degrees. Each measured dose presented in this work was converted to the quantity ambient dose equivalent per Joule at 1m from the target and the related uncertainty is estimated to be ~3%.

Results

From the dose measured by the TLD, it is possible to determine some of the characteristics of the X-ray and electron fields, such as the maximum energy and the angular distribution. Since the same target was shot several times (~32 shots per target), the dose measured represents an average. Even if the target and laser characteristics were kept constant during the irradiations, stochastic phenomena could affect the produced e⁻ and X-ray beams, causing a lower or higher dose on the TLDs in a single shot. Collecting more than 30 shots per target these random effects affect the measured dose at any angle, but the final contribution will be minimised.

We found that the divergence along the y-axis for all the irradiated targets was lower than the divergence on the x-axis. This can be seen in Fig. 2, where the dose (due to only photons emitted from the target) absorbed by the TLD chips of the outer ring on the laser plane, even by those placed at a large angle, was almost always higher than the dose absorbed by the TLDs below the laser plane, even if they were the stacks where, if placed on laser plane, a peak in the dose should have occurred. This is always verified for the doses measured from the first TLD chips of the stacks: the TLDs on laser plane were detecting much more low energy photons than the TLD chips below the plane. The doses due to the highest energy particles are instead seen to be almost similar at any angle.

At the same time, the divergence along the x-axis of both the electron and photon beams is shown to be very large and it

cannot be explained only by multiple scattering of the electrons inside the target: the electronic reflux was having a large effect on the electron beam spreading the particles at large angles on the laser plane. The measured dose due to electrons and photons is plotted in Fig. 3 as a function of the detection angle.

Focusing on the data from -40 to +60 degrees, this figure shows a large dose variation for all the TLDs in the stacks, but the dose trend changes with the depth in the stack. In the first plot representing the dose measured from the first TLD chips of the inner ring stacks we can see that the target producing the highest dose is 0.1mm Ta, this means that this target was emitting the less energetic particles stopped mainly in the first millimetres inside the stack. The least emitting target is instead the 3mm Ta. Looking at the dose measured from the second and the third TLD chips, the situation changes: now 1mm Ta is the most emitting target at all angles and SiO₂ is the least emitting one. This means that there are no more very low energetic particles and the intensity of the beam is gradually decreasing crossing the absorbers of the stack.

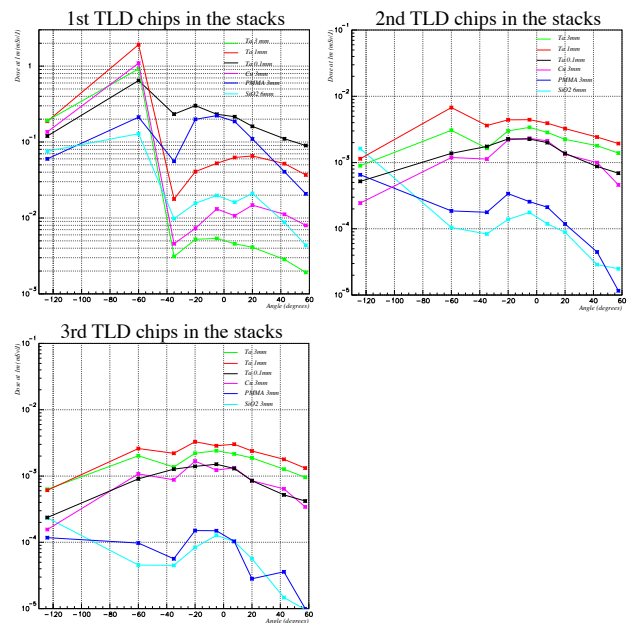


Fig.3 Dose measured in the TLD chips of the inner ring stacks as a function of the angle of detection.

Looking at the dose peaks in the graphs (mostly positioned

between -10 and 10 degrees) we can say that the main divergence of the beams is ~ 30 degrees, but the tails at large angles can only be explained with the effects of the electronic reflux inside the target. Any time the refluxing electrons reenter the target modify their divergence spreading inside the target.

From Fig.3 we can see that crossing the target for the first time, the electrons create a photon beam emitted with ~ 30 degree divergence: these photons together with the escaping electrons are the cause of the dose peak around 0 degrees. The lower tails at large angles must be due to the photons generated by the refluxing electrons (the number of which decrease at each target crossing). The very high peak at -60 degrees must also be caused by the reflux mechanism.

The irradiation of the PMMA target was repeated twice. In one case, the magnets in front of the outer ring stacks at 3 and 33 degrees were removed. This allowed us to determine the contribution to the dose due to the electrons at those angles and also to derive an estimate of the maximum electron energy. The comparison of the doses measured in presence and absence of magnets is shown in Fig.4. The doses due to electrons and X-rays measured in the first TLD of the stack at about laser axis appear to be almost two orders of magnitude higher than that measured in the case where the dose was due to only photons and in the case of the stack at about target normal the difference was almost an order of magnitude. This means that the electron beam divergence was lower than the divergence of the Xray beam, because the black curve is much higher in the first plot than in the second, but the red one doesn't show such a large reduction. Moreover, since for both the angles from the 4th TLD the dose due to e+X-rays is equal to the one due to only X-rays, we can assume that starting from somewhere in between the 3rd and the 4th TLD the totality of the electron beam and its secondary particles were stopped.

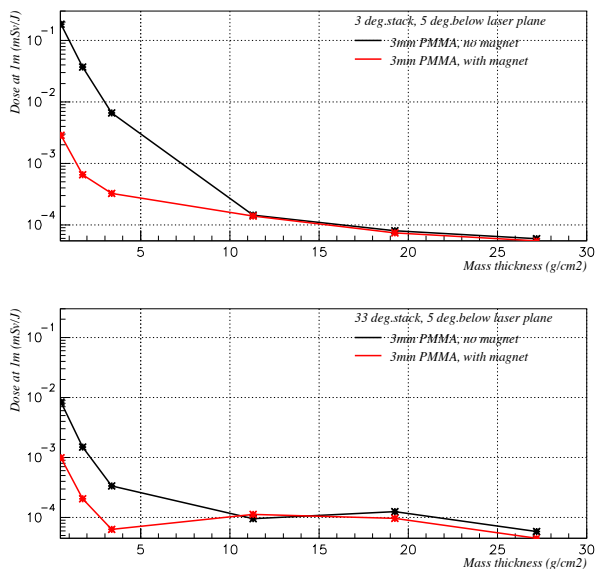


Fig.4 Comparison of the dose released by electron and photon beam (black curve) and the dose released by the only photon beam (red curve) on the TLD chips of the 3 (plot on the top) and 33 degree stacks. The doses were obtained shooting on 3 mm PMMA target, once with magnets installed in front of the stacks (red curve) and once without magnets (black curve).

Running a Monte Carlo simulation, using the FLUKA code [5, 6], of a monoenergetic electron beam crossing an outer ring

stack, we could determine the maximum energy of the electron beam created by the interaction of the laser with the plastic target. According the simulations, using an incident energy of (1.6 ± 0.2) MeV, the e^- beam and the secondary particles stop before hitting the middle of the 3rd TLD chip. Using instead an incident energy of (3.6 ± 0.1) MeV, the e^- beam and its secondary particles stop just before hitting the 4th TLD chip, so that there is no deposited energy on the 4th TLD of the stack. Thus the average maximum initial energy of the electrons escaping the target can be assumed as (2.6 ± 1.0) MeV.

Not having electrons reaching the 4th TLD of the outer stacks means that there are very few electrons reaching the 2nd TLD chips of the inner ring stacks (8.615 g cm^{-2}) and no electrons at all reaching the 3rd TLDs (16.555 g cm^{-2}). Looking also at the amount of the deposited dose, we can assume that at low mass thickness the deposition of energy is highly dominated by the electrons while at higher mass thickness ($\geq 10 \text{ g cm}^{-2}$) the energy deposition is dominated by the photons.

Running another Fluka simulation of the PMMA target and of an electron beam with a Maxwellian spectrum, it was possible to determine the $k_B T$ of the experimental initial beam knowing that the very maximum initial energy of the escaping electrons would have been 3.6 MeV.

Fig.5 (a) shows in black the spectrum of the electron beam generated by the laser in the front surface of the PMMA target if the spectrum followed a Maxwellian distribution and with maximum energies ≤ 3.6 MeV, and in red the distribution of the electrons at the rear surface of the target after having crossed the target thickness. The temperature of the initial electron beam is then determined to be ~ 0.38 MeV. As can be seen most of the initial electron beam is stopped in the target.

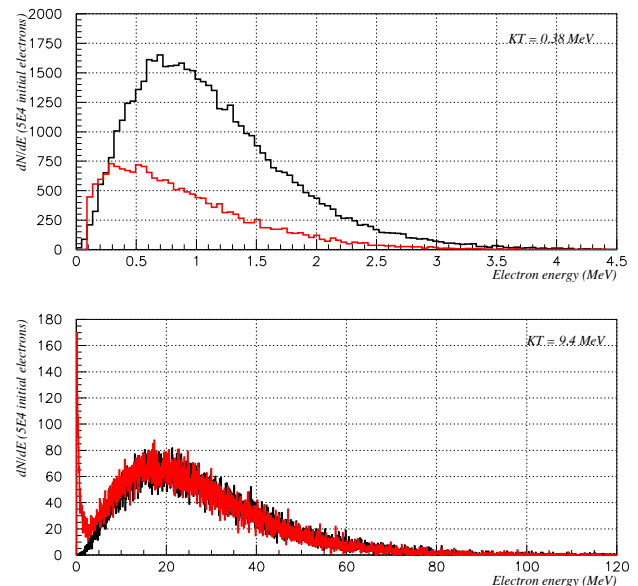


Fig.5 (a) In black it is shown the supposed Maxwellian spectrum of the created electron beam in the front surface of the target ($k_B T = 0.38$ MeV) obtained from the fact that the escaping electrons had a maximum initial energy between 1.6 and 3.6 MeV. The spectrum in red is the spectrum of the electrons at the rear surface of the target after having crossed the target. (b) In black it is shown the spectrum that according Wilks' theory the electron beam should have had ($k_B T = 9.4$ MeV) given our laser intensity. In red it is shown the consequent spectrum of the electrons at the rear surface of the target after having crossed the target.

This analysis assumes that the observed lower energy of the emitted electrons is accompanied by an electron spectrum within the target which has a much lower energy than would be predicted by Wilks' theory [7]. For our laser intensity this theory explains that the temperature of the generated electron beam should be ~ 9.4 MeV according to the equation:

$$k_B T \simeq 0.511 \left(\sqrt{1 + \frac{I \lambda^2}{1.37 \times 10^{18} \text{Wcm}^{-2} \mu\text{m}^2}} - 1 \right) \text{MeV}$$

Fig.5 (b) shows in black a Maxwellian energy distribution with $k_B T = 9.4$ MeV and in red the distribution of the electrons reaching the rear surface of the target after having crossed the target thickness.

Conclusions

From the dose released in the TLD chips we found out that the angular distribution does not match that reported in the literature: the divergence along both the x and y-axes is substantially different if compared to that reported in [8].

Further studies extending the covered angular range along the y-axis are required to characterise completely the electron and photon beams and better understand the effect of the reflux. In particular other measurements with and without magnets need to be performed to obtain separately the contribution to the dose due to the electron beam and the one due to the photon beam and once the electron spectrum is determined to fully understand the discrepancy with Wilk's theory in the beam temperature.

With regard to the targets, we can see that in order to obtain the largest number of emitted particles, not only the material is important but also its thickness. Several applications can be found using these beams and knowing the best targets to obtain the desired beam characteristics (spectrum, divergence and quantity of created particles) would be an advantage.

Acknowledgements

The work was funded by the LIBRA consortium grant from EPSRC, grant number EP/E035728/1.

References

1. AR Bell, JR Davies, S. Guerin, and H. Ruhl. *Fast-electron transport in high-intensity short-pulse laser-solid experiments*. Plasma physics and controlled fusion, 39:653, 1997.
2. J. Myatt, W. Theobald, JA Delettrez, C. Stoeckl, M. Storm, TC Sangster, AV Maximov, and RW Short. *High-intensity laser interactions with mass-limited solid targets and implications for fast-ignition experiments on OMEGA EP*. Physics of plasmas, 14:056301, 2007.
3. MN Quinn, XH Yuan, XX Lin, DC Carroll, O. Tresca, RJ Gray, M. Coury, C. Li, YT Li, CM Brenner, et al. *Refluxing of fast electrons in solid targets irradiated by intense, picosecond laser pulses*. Plasma Physics and Controlled Fusion, 53:025007, 2011.
4. S. Miljanic, M. Ranogajec-Komor et al. *Main dosimetric characteristics of some tissue-equivalent TL detectors*. Radiation protection dosimetry, 100:437-442, 2002.
5. G. Battistoni, S. Muraro, P.R. Sala, F. Cerutti, A. Ferrari, S. Roesler, A. Fasso', and J. Ranft. *The FLUKA code: Description and benchmarking*. Proceedings of the

Hadronic Shower Simulation Workshop 2006, Fermilab 6–8 September 2006, M. Albrow, R. Raja eds., AIP Conference Proceeding, 896:31–49, 2007.

6. A. Fasso', A. Ferrari, J. Ranft, and P.R. Sala. *FLUKA: a multi-particle transport code*, CERN-2005-10. INFN/TC 05/11, SLAC-R-773, 2005.
7. SC Wilks, AB Langdon, TE Cowan, M. Roth, M. Singh, S. Hatchett, MH Key, D. Pennington, A. MacKinnon, and RA Snavely. *Energetic proton generation in ultra-intense laser-solid interactions*. Physics of Plasmas, 8:542, 2001.
8. RD Edwards, MA Sinclair, TJ Goldsack, K Krushelnick, FN Beg, EL Clark, AE Dangor, Z Najmudin, M Tatarakis, B Walton. *Characterization of a gamma-ray source based on a laser-plasma accelerator with applications to radiography*. Appl. Phys. Lett. 80: 2129, 2002.

The Petatron: A high-rep rate combination diagnostic for laser-plasma experiments

Contact peta.foster@stfc.ac.uk

P S Foster*

Central Laser Facility, STFC Rutherford Appleton Laboratory
Chilton, Didcot, Oxon OX11 0QX, UK

*(Also at Centre for Plasma Physics, Queen's University
Belfast, Belfast BT7 1NN, UK)

D. Kiefer, J Schreiber

Max-Planck-Institute for Quantum Optics, Garching, Germany

T. Dzelzainis, M Yeung, B. Dromey, M. Zepf

Centre for Plasma Physics, Queen's University Belfast
Belfast BT7 1NN, UK

Introduction

The characterisation of high-intensity laser-plasma interactions is extremely challenging and normally relies on a combination of direct measurement of electron, ion and electromagnetic emission along with information gathered indirectly from interaction with probe beams of various types. Solid density thin foil experiments, often used in investigations into laser-driven ion acceleration [1,2] or the production of relativistic electron bunches suitable for flying mirrors [3] for example, rely primarily on the direct measurement of the accelerated ions and electrons respectively. To date spectra for ions and electrons as well as XUV emission have been made but either not on the same shot or not on the same line of sight. This implies that the data interpretation is strongly dependant on assumptions about the angular distribution and the shot-to-shot reproducibility. It is therefore highly desirable to devise a measurement system that would allow the simultaneous measurement of the ion/electron/XUV emission along the same line of sight, removing the assumptions about spatial distribution and shot-to-shot variability when comparing diagnostics. Here we present the development and testing of a new compact combination diagnostic, permitting just such a measurement, which has locally been dubbed the Petatron.

Diagnostic Overview

This diagnostic, as shown in figure 1, utilises a dual pinhole arrangement (2mm and 200µm) to enable the simultaneous use of a Lanex-screen for electron detection and an MCP for ion and soft-Xray detection, whereby the difference in pinhole size is chosen to compensate for the different sensitivity of the detectors. A 0.1T, 215mm in length, magnet was fielded in order to deflect the electrons upwards onto a Lanex screen inside the magnet body. The Lanex screen is shielded from extraneous light and is able to be adjusted vertically to enable selection of the range of electron energies being detected. This Lanex screen is then imaged onto an Electron Multiplying CCD (EMCCD) through a window. The ions travelling through both pinholes were deflected downwards and in order to resolve the different species electric field plates were included. An aluminium beam dump excluded the large pinholes ion track from propagating through the electric field plates and therefore only one set of non-saturated tracks were detected. A 1000lines/mm Gold grating was positioned behind the electric plates, along the line of sight to the target in order that the light observed could be spectrally resolved and detected by the MCP. A compact spatial ion beam profiler was installed in front of the overall system, to provide a shot-to shot monitor of overall direction of the ion beam.

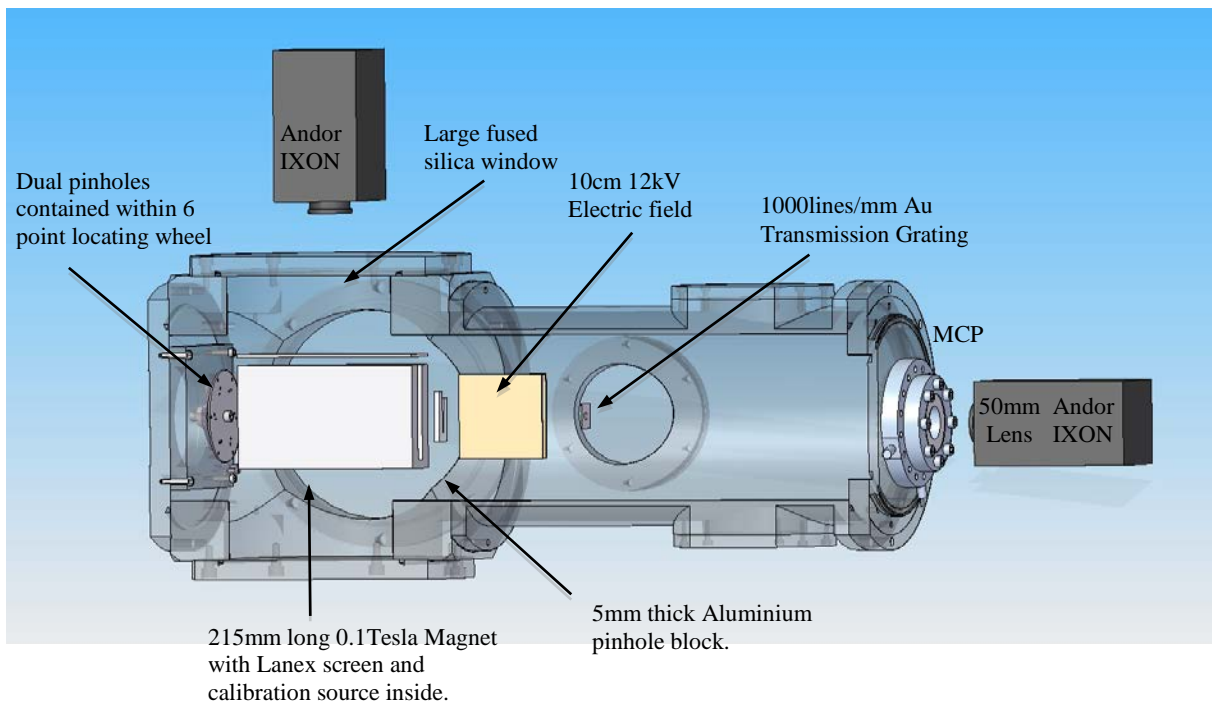


Fig. 1. A schematic diagram of the Petatron, depicting from left to right the rotating pinhole wheel; the 215mm long 0.1Tesla magnet with a Lanex screen (seated inside the magnet unit) with a window and imaging camera directly above, outside the chamber; an aluminium ion block for the 2mm pinhole; the 12kV Electric field plates (10mm internal gap); a 10mm aperture 1000lines/mm freestanding Gold transmission grating placed along the line of sight; A 77mm diameter Hamamatsu MCP imaged by a 50mm Nikon lens couple to a Andor Ixon EMCCD.

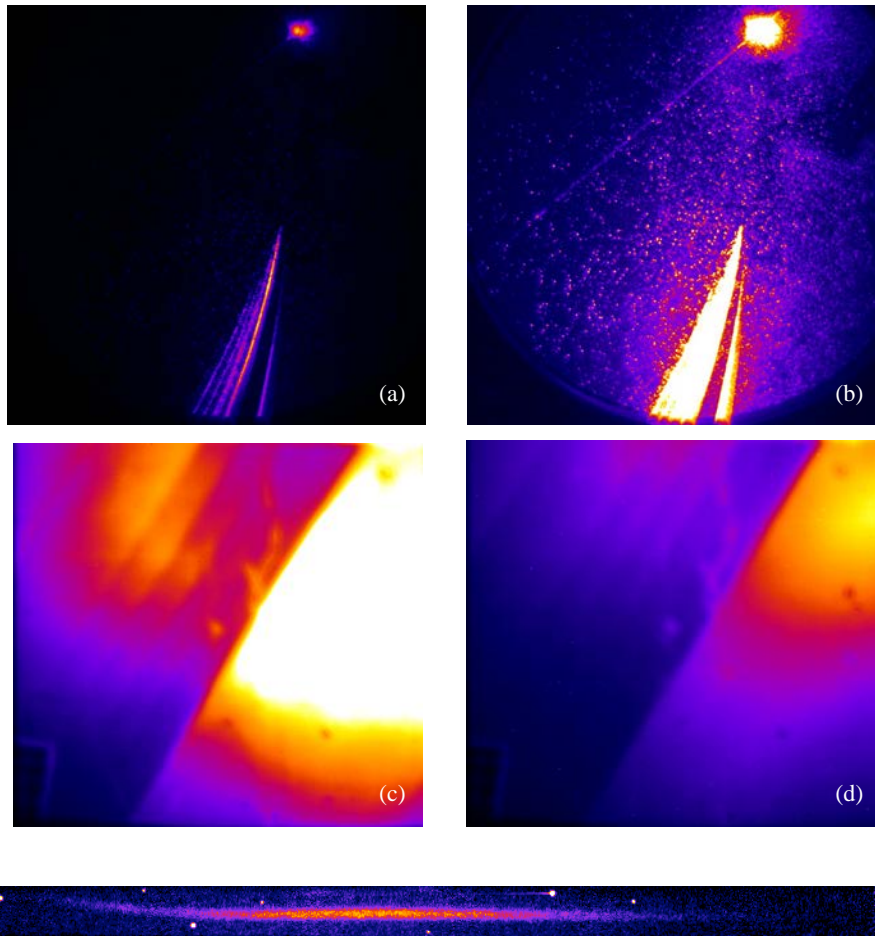


Fig. 2. A sample of the data that can be acquired simultaneously using this diagnostic. (a) and (b) display the imaged MCP. (a) clearly shows the resolved ion species tracks in the lower half of the image and at the top the zero deflection point. (b) has been scaled such that the soft x-ray spectra ranging from 10-100nm can be seen emerging from the zero point. Also in the top right of the image the shadow of the diffraction grating holder can be seen. (c) and (d) show the image from the compact ion beam spatial profiler for two different shots, with filter pack able to resolve from 1 to 5MeV. (e) shows an example electron spectra acquired.

Detector Design

Dual Pinhole

The dual pinholes are separated by 7mm diagonally to allow maximum range for the ion and EUV spectra. To allow for the possible changes in flux with different targets, 6 different pinhole size combinations were mounted on a locating rotating wheel. The pinholes are backed with individual lead collimators to reduce hard x-ray shot noise.

Magnetic and Electric Fields

The magnet was 215mm in length (l_m) and 0.1Tesla in field strength (B). The electric plates were 100mm by 100mm and had a separation of 10mm. The ion trajectories can easily be determined by the equations of motion of a charged particle through an external electric and magnetic field, as given by the Lorentz force:

$$F = q(E + v \times B) \quad (1)$$

producing a function of ion energy with respect to deflection:

$$E_{ion} = [qBl_m(l_m/2 + l_d)]^2 / 2m_i y \quad (2)$$

where l_d is the distance between the magnet and the detector, l_m is the magnet length and y is the magnetic deflection at the detector plane. The electric deflection separates the ion species and allows for species identification.

Microchannel plate

This 77mm diameter MCP was operated with an average voltage of -1.1kV and +3.3kV. The chamber was operated at a chamber pressure of 10^{-6} mbar which was achieved using a turbo pump directly connected to the chamber and differential pumping. A cold finger was also implemented to speed up pump down times.

Compact spatial beam profiler.

In order to allow numerous other diagnostics to work in parallel this detector was designed to be as compact as possible. This section of the diagnostic comprised of a 1mm thick calibrated BC422Q plastic scintillator [4], manufactured by Saint-Gobain Crystals that was flash coated with aluminium to minimise light leaks. This was mounted at the end of a 20cm long tapered light tight box that housed a TV lens which imaged the emission at the back of the scintillator. From the images in figure 2c and 2d it can be seen that the detector was mounted with the top-left corner injected close to the centre of the ion beam cone. 2 full layers of 5um thick aluminium were applied over the end of the scintillator box to prevent laser and other visible light emission from being detected. Since the scintillator is 1mm thick it is sensitive to all protons up to around 10MeV as well as electrons and x-rays and so a filter pack consisting of 6 layers, each increasing the attenuation by 20um Aluminium, were added over half the detector area to provide some energy resolution. This can be seen in the top right of images 2c and 2d. The

image from the scintillator was coupled to an EMCCD via an 8mm square fibre optic taper to maximise the light collection.

Detection Range

The detector was designed to operate in the ranges that were expected from the interaction of the Astra Gemini laser with various nanometre scales foils, show in figure 3, whilst allowing for higher energy ions to be resolved should they appear.

Ions	4-50 MeV
Electrons	0.2-20 MeV
Soft x-ray -EUV	10-110 nm
Ion angular distribution sample (Integrated over 1-10MeV)	14 degrees from beam axis

Fig. 3. Table of required simultaneous measurements.

The diagnostic can be readily adjusted to tune different ranges. The position of the lanex can be used to view different electron energy ranges. The position of the grating can be modified to tune the EUV range and the ion spectra can have increased dispersion by adding an additional dispersive magnet. The ion angular distribution can be increased by adjusting the position of the footprint monitor with respect to the interaction point and also expanding the size of the scintillator.

Future Plans

This detector proved very valuable to the experiment in terms of enabling the simultaneous measurement of a number of desirable parameters that would otherwise not be explored, however there are a number of obvious lines for potential improvements. These include adding a scintillator channel to the large pinhole line to allow collection of data at lower ion energies while retaining the high dispersion and resolution on the MCP; providing a cut-away to allow for the detection of positrons; shaped electric field plates to allow a higher separation between species at the higher energies; motorisation of the pinhole wheel to allow remote control of the detector flux level and the easy addition of further magnet sections for the resolution of very high-energy ions.

Acknowledgements

We would like to acknowledge Pete Brummitt and Darren Neville for their help in the pinhole design and assembly of the spectrometer and Steve Hook for the production of the schematic images contained within this report.

References

1. 'Enhanced proton beams from ultrathin targets driven by high contrast' D. Neely, Appl. Phys. Lett. 89, 021502 (2006)
2. "Relativistically correct hole-boring and ion acceleration by circularly polarized laser pulses" A P L Robinson et al Plasma Phys. Control. Fusion 51 024004 (2009)
3. "First observation of quasi-monoenergetic electron bunches driven out of ultra-thin diamond-like carbon (DLC) foils" D. Kiefer Eur. Phys. J. D 55, 427-432 (2009)
4. "Characterisation of plastic scintillators for detection of laser-accelerated protons " J Green et al CLF Annual Report 2010-2011

Measurement of laser-generated electron slope temperature using electron stopping

Contact: krygier.5@osu.edu

A.G. Krygier

*The Ohio State Univ.
Physics Department
Columbus, OH 43210, USA*

R.B. Stephens, G. Lee, N. Alexander

*General Atomics
PO Box 85608
San Diego, CA 92121, USA*

D. Symes, K. Markey

*STFC
Rutherford Appleton Lab, Chilton
Didcot, Oxfordshire, OX11 0QX UK*

Introduction

Measurements of $K\alpha$ fluorescence from buried layers of Ni and Cu have been used to investigate the energy of laser-generated hot electrons by characterizing their transport range. The x-ray emissions were recorded using a cylindrically bent crystal HOPG spectrometer. The approximate slope temperature of the hot electrons, T_e , and its variation with laser intensity, I_L , are inferred from the relative fluorescence intensities of the buried layers at different depths. The Monte Carlo code MCNP is used to model the transport of the hot electrons and infer T_e . Simulations using non-relativistic calculations of the electron source and the hybrid PIC code LSP will be necessary to properly simulate the experimental results. Extensions of this experimental work combined with modeling have the potential to further reveal the basic physics of how hot electrons transport solid materials.

Experimental Setup

The experimental campaign was carried out at the Astra-Gemini laser at Rutherford Appleton Laboratory (RAL). Both beams were used; one delivered up to 12J of 800nm light in a 300fs (expanded from 50fs) beam focused with an $f/20$ off-axis parabola incident on the target at an angle $\sim 10^\circ$. The $\sim 25 \mu\text{m}$ diameter focal spot resulting from the $f/20$ mirror gave a pulse (calculated) intensity of $\sim 10^{18} \text{ W/cm}^2$ which produced the non-thermal fast electrons. The other beam, 800nm 50fs, delivered 0-300mJ, focused with a 3.5m focal length spherical lens to $30 \mu\text{m}$, was timed to arrive $\sim 1\text{ps}$ in advance of the main pulse to provide a controlled pre-plasma. The Astra-Gemini laser is capable of delivering full-power shots at a repetition rate exceeding one shot per minute. Laser pulse energy and focus were recorded shot-by-shot.

Four types of targets were used; so-called “refluxing” and “non-refluxing” each with either rough ($\sim 1 \mu\text{m}$ rms) or smooth ($\ll 1 \mu\text{m}$ rms) front surfaces. Each target had a $4 \mu\text{m}$ Al front layer, $36 \mu\text{m}$ Ni middle layer, and $10.9 \mu\text{m}$ Cu back layer. Layer thicknesses were controlled to $\pm 4\%$. The refluxing targets were large foils (100 targets per foil) sandwiched in a target holder with 1mm diameter holes on the front and back. The non-refluxing targets were $700 \mu\text{m}$ diameter discs glued to a $50 \times 50 \times 1 \text{mm}^3$ C “electron get-lost layer”; 100 disc foils were glued to each get-lost layer. A measurement of the average fluorescence yield from these layers with good statistics is made possible by taking repeated shots on nearly identical targets; over 200 shots were taken in this campaign.

Two cylindrically bent von Hamos HOPG crystal spectrometers were used to relay the Cu- $K\alpha$ and Ni- $K\alpha$ emissions to a single Andor x-ray CCD whose quantum efficiency was $\sim 20\%$. The images appear as out-of-focus arcs because of the different focal lengths of the two spectrometers (Fig. 1).

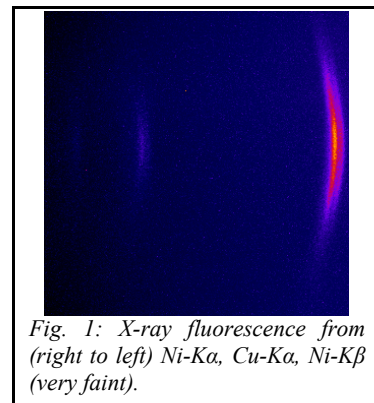


Fig. 1: X-ray fluorescence from (right to left) Ni- $K\alpha$, Cu- $K\alpha$, Ni- $K\beta$ (very faint).

Results/Analysis

$K\alpha$ emissions from the Ni and Cu foils have similar absorption in both Ni and Cu, so the observed Ni- $K\alpha$ to Cu- $K\alpha$ yield ratio is a measure of the electron current at the end of the Ni foil relative to that in the Cu foil. Calculations of this ratio using the Monte Carlo code MCNPⁱ to model the electron propagation through the foils as a function of electron slope temperature (Fig. 2) show the dependence of this ratio with range. The ratio is ~ 2 for high energy electrons; in that case the current flowing through the layers are nearly equal, as one would expect for electrons with range longer than the foil thickness. The ratio is seen to be larger for $T_e < 100$ keV, for which the electrons reach their maximum depth near the Ni-Cu boundary, and only a few get into the Cu. The experimental data (Fig. 3) show ratios corresponding to a slope temperature near $T_e \sim 50$ -60 keV.

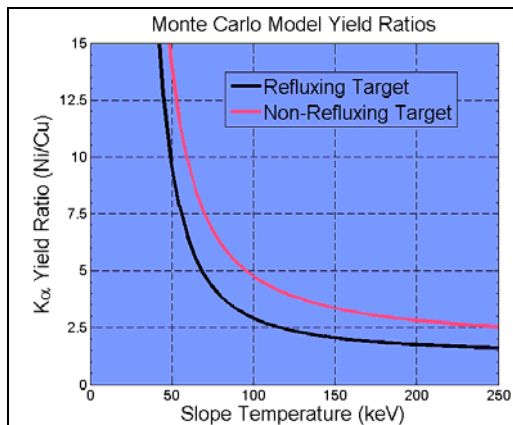


Fig. 2: Fluorescence yield ratio predicted by MCNP modeling.

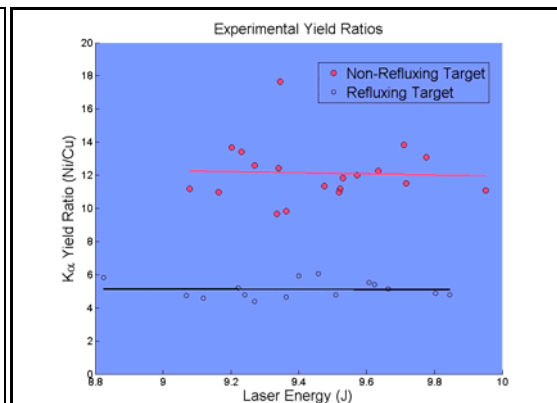


Fig. 3: Ratio of $K\alpha$ yields from Ni and Cu foils vs. laser intensity. The ratio would be ~ 2 if the current through the two layers were the same.

Discussion

The results of the Monte Carlo model suggest that the slope energy of the electron distribution is ~ 50 -60 keV, much different than the ~ 200 keV predicted by extrapolating from the ponderomotive scalingⁱⁱ. This is not surprising, considering that the ponderomotive scaling was postulated by Wilks in a region of intensities where relativistic effects dominate, at least an order of magnitude greater than the intensities we estimate were used in our experiments. We note that Monte Carlo models simulate the transport of many particles, one at a time, through the target but includes only scattering and x-ray radiation production, with no physics model of current effects: e.g. “Ohmic” fields are not included. More sophisticated modeling using the hybrid PIC code LSPⁱⁱⁱ will be necessary for a proper simulation of the experiment. In this advanced treatment, no assumption is made of the slope temperature of the generated fast electrons as the simulation will model the laser-plasma interaction and the electron transport, including collective effects such as fields, and escaping particles; $K\alpha$ generation in LSP is modeled with ITS^{iv} libraries.

Summary

Initial Monte Carlo analyses are not sufficient to explain the higher-than-expected observed fluorescence intensity ratio. This difference is likely due to the naïve assumptions of the electron source characteristics, and lack of self-consistent electric fields, all problems which are correctly modeled by LSP. Combining such analyses with experimental data similar to those presented here will be useful as an in situ measure of laser-generated electron spectra, particularly to examine predicted variations in the high energy tail of the distribution with pre-pulse variations.

Acknowledgements

The generous extra efforts of the Astra-Gemini staff who facilitated this experiment are greatly appreciated. This campaign was supported by the OFES through DOE under contract no. DE-FG02-05ER54834, and by the corporate support of General Atomics.

ⁱ X-5 Monte Carlo Team, "MCNP - A General N-Particle Transport Code, Version 5 - Volume I: Overview and Theory", LA-UR-03-1987, Los Alamos National Laboratory (2003)

ⁱⁱ S.C. Wilks, et al., *Phys. Rev. Lett.* **69** 1383-1386 (1992).

ⁱⁱⁱ D.R. Welch, et al., *Phys. Of Plasmas* 13, 063105 (2006)

^{iv} J.A. Halbleib, et al., "ITS Version 3.0: The integrated TIGER Series of Coupled Electron/Photon Monte Carlo Transport Codes," Technical Report SAND91-1634, Sandia National Laboratories (1992)

Relativistic high-order harmonics from gas jets and their power scaling

A. S. Pirozhkov, M. Kando, T. Zh. Esirkepov,
 A. Ya. Faenov, T. A. Pikuz, T. Kawachi, A. Sagisaka,
 J. K. Koga, M. Mori, K. Kawase, T. Kameshima,
 Y. Fukuda, L. Chen, I. Daito, K. Ogura, Y. Hayashi,
 H. Kotaki, H. Kiriya, H. Okada, T. Imazono, K. Kondo,
 T. Kimura, T. Tajima, H. Daido, Y. Kato, S. V. Bulanov
 Advanced Beam Technology Division, Quantum Beam Science
 Directorate, JAEA
 8-1-7 Umemidai, Kizugawa-city, Kyoto 619-0215, Japan

P. Gallegos, J. Green, P. Foster, C. Brenner, D. R. Symes,
 P. Rajeev, D. Neely
 Central Laser Facility, STFC Rutherford Appleton Laboratory
 Chilton, Didcot, Oxon OX11 0QX, UK

M. Coury, P. McKenna
 University of Strathclyde, Department of Physics, SUPA
 Glasgow G4 0NG, UK

H. Ahmed, B. Dromey, M. Borghesi
 Centre for Plasma Physics, Queen's University Belfast
 Belfast BT7 1NN, UK

E. N. Ragozin
 P. N. Lebedev Physical Institute of the Russian Academy of
 Sciences
 53 Leninsky Prospekt, Moscow 119991, Russia

N. Nishimori
 Laser Application Technology Division, JAEA
 2-4 Shirakata-Shirane, Tokai, Naka, Ibaraki 319-1195, Japan

Introduction

We have recently [1, 2] experimentally observed the generation of odd and even high order harmonics with smooth and modulated spectra from the relativistic laser – gas jet interactions. To explain these, we introduce and discuss a new harmonic generation mechanism. In this Paper we describe an experiment [2] performed with Astra Gemini laser [3], where we demonstrate that the harmonics are generated with linearly as well as circularly polarized pulses, have the angular distribution with the width of a few degrees, and the emitted photon number with the laser power of 120 TW is ~ 2 orders of magnitude greater than in the previous experiment performed with the 9 TW laser.

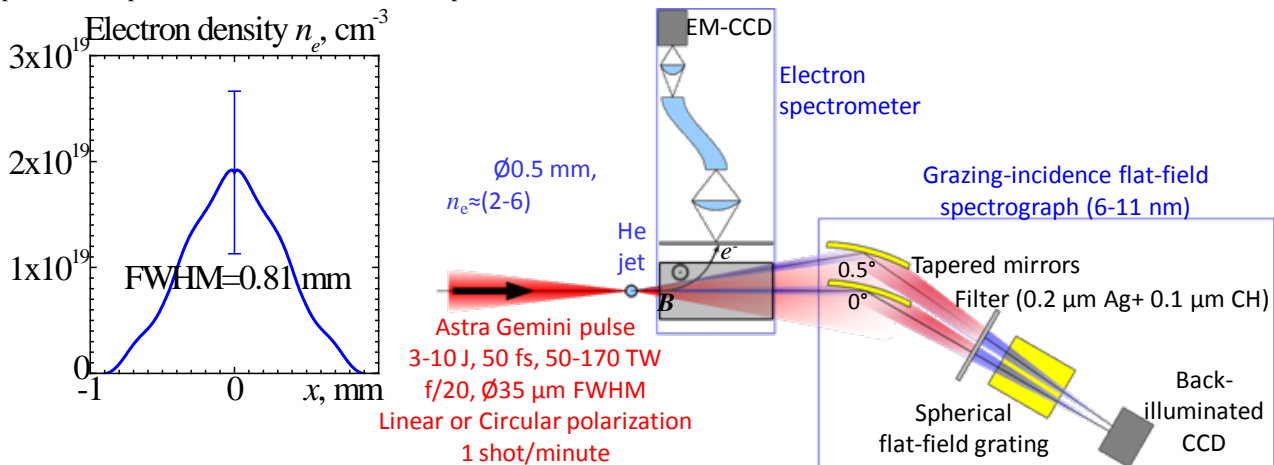
Experiment

The experimental setup schematic is shown in Fig. 1. Laser pulses from Astra Gemini laser are focused by an $f/20$ off-axis parabola into a 0.5 mm diameter Helium gas jet. The laser pulse has a duration of 50 fs, an energy of 7 J, a power of 120 TW, giving an estimated vacuum irradiance of 4×10^{18} W/cm². The harmonics are observed with a two-channel grazing-incidence flat-field spectrograph [4] comprising two tapered ellipsoidal gold-coated mirrors, 200 nm thick silver optical blocking filter on 100 nm CH substrate, flat-field diffraction grating, and back-illuminated CCD. The two spectrograph channels observe the harmonics source on-axis and slightly off-axis, 0.5° in the polarization plane for the shots with linear polarization. The

spectrograph is operated in the 2nd and 3rd diffraction orders to reduce the amount of scattered light. The wavelength calibration is performed in-place using Neon plasma emission. The absolute photon yield is estimated using the known acceptance angle and idealized throughput, i.e. the product of the calculated [5] collecting mirror reflectivity and filter transmission, measured diffraction grating efficiency [6], and manufacturer-provided CCD efficiency. The high-energy (>100 MeV) electrons accelerated in the gas jet are deflected out of the flat-field spectrograph by a permanent magnet and analysed with the electron spectrometer.

Harmonic generation by linearly and circularly polarized pulses

The harmonics are generated in a wide range of peak plasma densities from $\sim 1.7 \times 10^{19}$ to $\sim 4.5 \times 10^{19}$ cm⁻³. Typical single-shot raw data are shown in Fig. 2. With the linearly polarized pulses, both the odd and even harmonics with down-shifted base frequency are detected, Fig. 3, with deep equidistant spectral modulations in some shots. These features are consistent with those observed in [1]. In addition, we observed similar harmonics spectra with circularly polarized laser pulses, Fig. 2 (b) and Fig. 3 (b). However, in ~ 90 shots with the circular polarization the large-scale spectral modulations have not been observed.



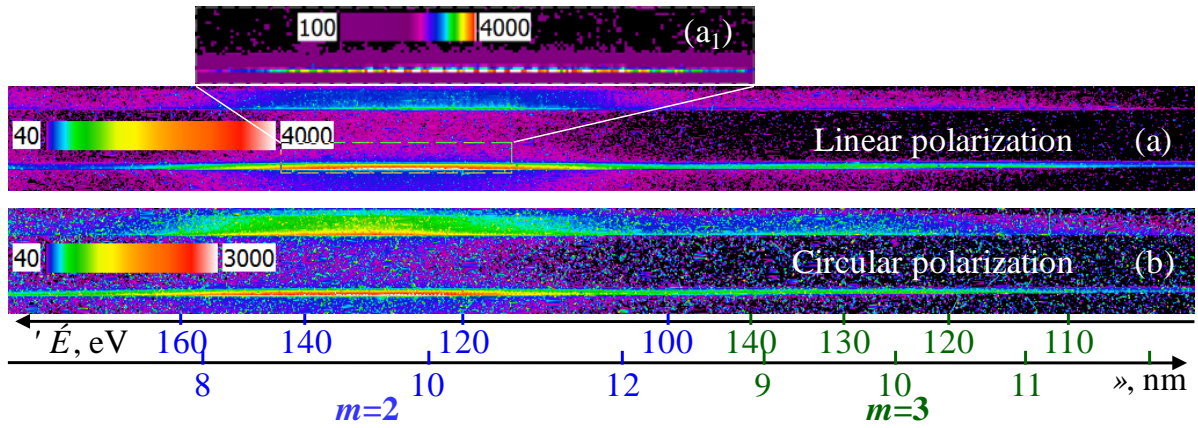


Fig. 2. Examples of raw data obtained with linearly (a) and circularly (b) polarized pulses; m denotes the diffraction order. The inset (a) shows close-up with resolved harmonics.

The harmonic structures and base frequencies obtained from the 2nd and 3rd diffraction orders nearly coincide, while the spectral intensities differ by 12% only, Fig. 3 (a). These serve as additional confirmations of the correct wavelength calibration and throughput calculation. The highest resolved harmonic orders recorded are about 370, Fig. 3 (b).

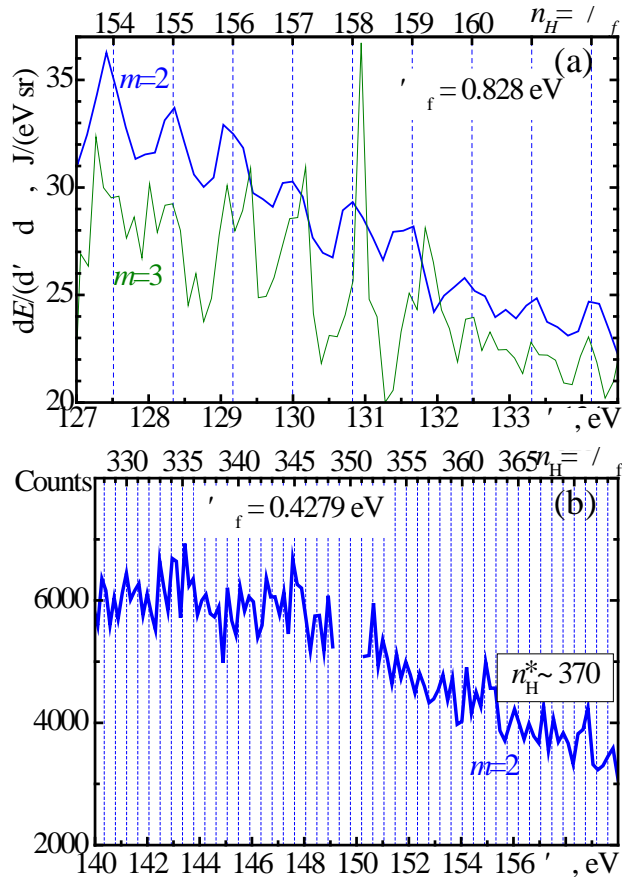


Fig. 3. (a) Spectrum obtained from the 2nd and 3rd diffraction orders of the shot shown in Fig. 2 (a) using idealized spectrograph throughput. (b) Narrow (3-pixel wide) lineout of the raw data shown in Fig. 2 (b) with resolved harmonic orders up to ~ 370 . In (a) and (b) the top axes show the harmonic order $n_H = \hat{E}/\hat{E}_f$, where \hat{E}_f is the base harmonic frequency.

Angular distribution

Two spectrograph channels observing the harmonics on-axis and $\sim 0.5^\circ$ off-axis show spectra with similar intensity, taking into account ~ 2.5 -fold difference in the acceptance angles determined from the nearly isotropic Neon plasma emission, Fig. 4. However, in some shots one of the channels show

several times greater signal than another. These observations indicate that the angular distribution of the harmonic emission has a characteristic size of a few to several degrees and there are few-degree direction fluctuations. Comparison with the high-resolution 2D PIC simulations performed with the code REMP [7], see below, suggests that the harmonics are emitted slightly off-axis and for harmonic orders about hundred the angular width of the lobes is $\sim 3^\circ$ [8].

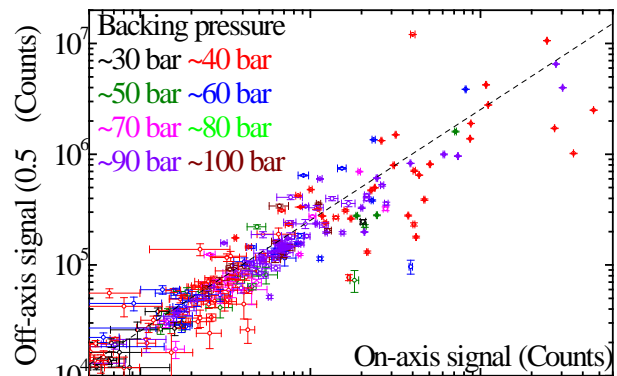


Fig. 4. Comparison of total signals recorded with various experimental parameters by the on-axis and off-axis channels, the colour encodes the He backing pressure. In majority of the shots, the signal ratio of the two channels is close to the acceptance angle ratio (slope of the dashed line), although in some shots the signal ratio deviates from the general trend.

Power scaling

One harmonic at 120 eV contains (per unit solid angle) 2×10^{12} photons/sr and 40 J/sr (Fig. 5). Using the angular width of 3° found in the previous section, we can estimate the total yield per harmonic per shot as 4×10^9 photons and 90 nJ. The comparison of several strongest harmonic spectra obtained with 7 J, 120 TW and 0.4 J, 9 TW laser pulses shown in Fig. 5 indicates that the achievable photon number is scalable with the driving laser energy and power. Taking into account many possibilities for the harmonic signal optimization which are not yet explored and the quick grows of the available femtosecond laser power, we believe that the relativistic harmonics generated in underdense plasmas may become one of the strongest available coherent XUV and soft X-ray sources.

New harmonic generation mechanism

The observed harmonics cannot be explained by previously known scenarios. Atomic harmonics are excluded because both odd and even harmonic orders with a weak sensitivity to gas pressure are observed using linearly and circularly polarized

pulses. Betatron radiation is not relevant because the base frequency of its harmonics is determined by the plasma frequency and electron energy, not the laser frequency. The nonlinear Thomson scattering cannot provide the observed photon numbers even under the most favourable assumptions. Based on the experimental observations and extensive 2D and 3D PIC simulations [7], we introduce a new mechanism, in which the harmonics are collectively emitted by oscillating electron spikes, which are cusp singularities formed at the joints of two lower-order fold singularities, the boundaries of a cavity and bow wave created by a relativistically self-focusing laser in underdense plasma, Fig. 6. The spike sharpness and stability are explained by catastrophe theory [9]. The high-resolution 2D PIC simulation performed with the parameters close to the experiment with Astra Gemini laser, Fig. 7, shows harmonics spectra consistent with the experimentally observed.

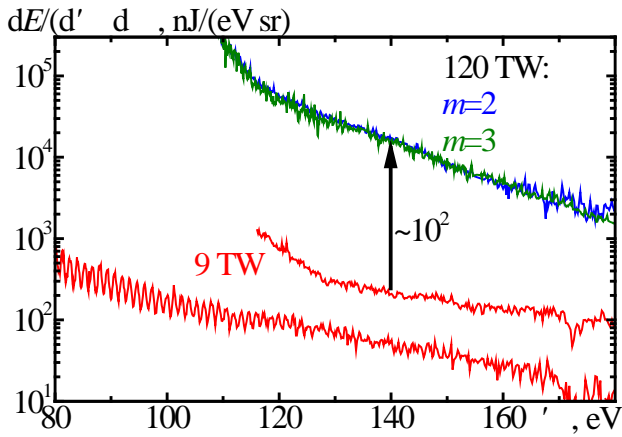


Fig. 5. Comparison of representative strongest spectra obtained in the experiments with 0.4 J, 9 TW J-KAREN and 7 J, 120 TW Astra Gemini lasers [for 120 TW, the same shot is shown as in Fig. 2 (a) and Fig. 3 (a)].

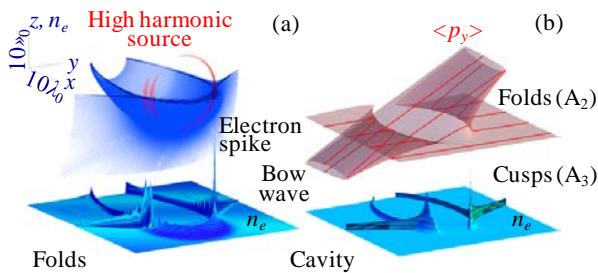


Fig. 6. 3D PIC simulation (a) and model (b) of relativistic high-order harmonic generation in underdense plasma.

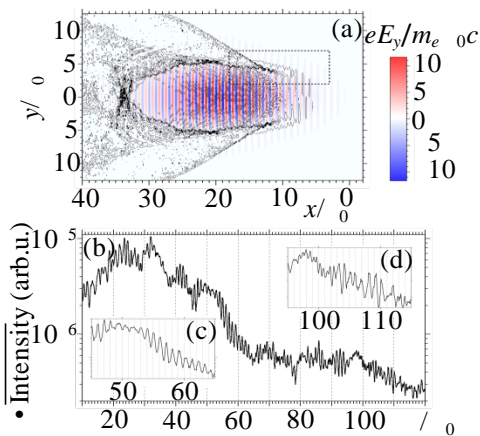


Fig. 7. 2D PIC simulations with the parameters close to the experiment with Astra Gemini laser. (a) Electron density (black) and laser field (colour). (b-d) Harmonics spectrum in the region shown in (a) by the dotted rectangle.

Conclusions

We experimentally studied properties of high-order harmonics generated in gas jet with relativistic-irradiance laser. We demonstrate that the harmonics are generated by linearly and circularly polarized pulses, extend to orders of at least ~ 370 , and have the angular distribution width of a few degrees. Using 120 TW pulses from Astra Gemini laser, we demonstrate that the harmonic yield is scalable with the laser power, and reaches ~ 90 nJ in one harmonic at 120 eV. Our findings may open way to a next-generation compact coherent X-ray source realizable with a university laboratory scale repetitive laser and accessible, replenishable and debris-free gas jet target.

Acknowledgements

We acknowledge the financial support from MEXT (Kakenhi 20244065, 21604008, 21740302, and 23740413), JAEA President Grant, and STFC (facility access funding).

References

1. A. S. Pirozhkov, M. Kando, T. Zh. Esirkepov, E. N. Ragozin, A. Ya. Faenov, T. A. Pikuz, T. Kawachi, A. Sagisaka, M. Mori, K. Kawase, J. K. Koga, T. Kameshima, Y. Fukuda, L.-M. Chen, I. Daito, K. Ogura, Y. Hayashi, H. Kotaki, H. Kiriya, H. Okada, N. Nishimori, K. Kondo, T. Kimura, T. Tajima, H. Daido, Y. Kato, S. V. Bulanov, "X-ray harmonic comb from relativistic electron spikes," *arXiv:1004.4514v1* (2010).
2. A. S. Pirozhkov, M. Kando, T. Zh. Esirkepov, P. Gallegos, H. Ahmed, E. N. Ragozin, A. Ya. Faenov, T. A. Pikuz, T. Kawachi, A. Sagisaka, J. K. Koga, M. Coury, J. Green, P. Foster, C. Brenner, B. Dromey, D. R. Symes, M. Mori, K. Kawase, T. Kameshima, Y. Fukuda, L. Chen, I. Daito, K. Ogura, Y. Hayashi, H. Kotaki, H. Kiriya, H. Okada, N. Nishimori, T. Imazono, K. Kondo, T. Kimura, T. Tajima, H. Daido, P. Rajeev, P. McKenna, M. Borghesi, D. Neely, Y. Kato, and S. V. Bulanov "Soft X-ray harmonic comb from relativistic electron spikes," (submitted to *Phys. Rev. Lett.*).
3. C. J. Hooker, J. L. Collier, O. Chekhlov, R. Clarke, E. Divall, K. Ertel, B. Fell, P. Foster, S. Hancock, A. Langley, D. Neely, J. Smith and B. Wyborn, "The Astra Gemini project - A dual-beam petawatt Ti:Sapphire laser system," *J. Phys. IV France* **133** 673-677 (2006)
4. D. Neely, D. Chambers, C. Danson, P. Norreys, S. Preston, F. Quinn, M. Roper, J. Wark, and M. Zepf, "A multi-channel soft X-ray flat-field spectrometer," *AIP Conf. Proc.* **426**, 479 (1998)
5. B. L. Henke, E. M. Gullikson, and J. C. Davis, "X-Ray Interactions: Photoabsorption, Scattering, Transmission, and Reflection at $E = 50$ -30,000 eV, $Z = 1$ -92," *At. Data Nucl. Data Tables* **54**, 181-342 (1993); R. Soufli, and E. M. Gullikson, "Optical constants of materials for multilayer mirror applications in the EUV/soft x-ray region," *Proc. SPIE* **3113**, 222-229 (1997); <http://henke.lbl.gov/optical/textunderline constants/>
6. T. Imazono, K. Sano, Y. Suzuki, T. Kawachi, and M. Koike, "Development and performance test of a soft x-ray polarimeter and ellipsometer for complete polarization analysis," *Rev. Sci. Instr.* **80**, 085109-8 (2009).
7. T. Zh. Esirkepov, "Exact charge conservation scheme for Particle-in-Cell simulation with an arbitrary form-factor," *Comput. Phys. Comm.* **135**, 144-153 (2001).
8. P. Gallegos *et al.*, in preparation.
9. T. Poston and I. Stewart, *Catastrophe theory and its applications* (Dover, 1996).

Characterization of temporal contrast following a double plasma mirror system

D. R. Symes, K. Poder, P. S. Foster, N. Booth, Y. Tang, O. Chekhlov, S. J. Hawkes & P. P. Rajeev

Central Laser Facility, Rutherford Appleton Laboratory, Didcot, OX11 0QX

B. Dromey, D. Kiefer, T. Dzelzainis, M. Yeung, T. Marshall & M. Zepf

School of Mathematics and Physics, Queen's University Belfast, University Road, Belfast BT7 1NN, UK

Introduction

Many of the experiments performed using intense short pulse lasers require an exceptionally high level of pulse contrast. With short focal length optics (e.g. an $f/2$ off axis parabola) the Astra-Gemini laser can generate a focused intensity approaching 10^{22} Wcm^{-2} . Most materials ionize close to an intensity of 10^{13} Wcm^{-2} so for the main pulse to interact with an undisturbed target the contrast must be $\sim 10^9$ on a sub-picosecond timescale. This is crucial for cutting edge experiments such as harmonic generation from solid surfaces [1] and ion acceleration from ultra-thin foils [2]. A certain level of light before the main pulse is inherent to chirped pulse amplification laser systems as discussed in detail elsewhere in this annual report [3].

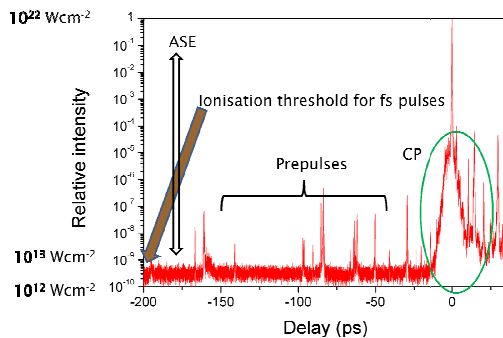


Figure 1. A typical contrast trace from Astra-Gemini. The peak intensity and typical ionisation threshold are indicated. Also indicated are the three features of the contrast trace: ASE background, prepulses and the coherent pedestal.

In a typical contrast trace from Astra-Gemini (shown in Fig 1), although the baseline level from amplified spontaneous emission is very low at $<10^{-9}$, we identify discrete prepulses on the timescale of tens of picoseconds and a coherent pedestal [4] starting to rise at ~ 20 ps. The pre-pulses here, which originate from post-pulse conversion [4, 5], are being systematically identified and eliminated. However, at present there is no known technique for removing the coherent pedestal and for the foreseeable future it will be necessary to perform contrast enhancement using plasma mirrors.

Plasma mirror system in Target Area 3

In the Astra-Gemini target chamber there is a compact plasma mirror (PM) arrangement for use on experiments demanding the highest levels of contrast. This has been described in a previous report [6] and a diagram is shown in Fig. 2. In this system the beam is focused and recollimated by two $f/7$ parabolic mirrors. To act as PMs, rectangular anti-reflection coated windows are placed either side of the focus where the intensity is $\sim 10^{15}$ Wcm^{-2} . High reflectance bypass mirrors can be driven in when the plasma mirrors are not required. In theory, before the laser intensity reaches the ionization threshold of the PM ($\sim 10^{13}$ Wcm^{-2}) the laser is attenuated by a factor of $\sim 10^4$. At the onset of ionization the substrates become reflective transmitting

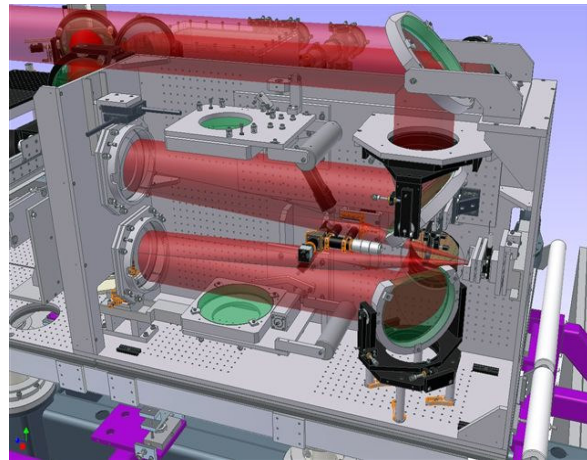


Figure 2. The double plasma mirror system employed in the Astra-Gemini target area for contrast enhancement.

$\sim 70\%$ of the laser energy per PM and maintaining the beam profile. Such PMs are commonly employed to prevent amplified spontaneous emission, low level prepulses and the coherent pedestal from reaching the target. In this work we have directly measured the pulse contrast after the plasma mirrors.

Measurement of pulse contrast

Ordinarily the contrast of the laser is measured using a scanning third order autocorrelator building up a contrast trace over many shots as the delay between the fundamental and second harmonic is changed. On Astra-Gemini we employ a commercial device (Amplitude Sequoia [7]) and average 10 shots for each delay position with the laser operating at a 10 Hz repetition rate. A scan with the 10Hz beam from -20 ps to $+20$ ps is shown in Fig. 3 (grey line). We also scanned around -30 ps and -90 ps where we have known prepulses. To characterize the full power laser it is necessary to perform this same task with laser shots once per minute so we reduced each data point to an average of only two shots. This worked surprisingly well and the full power Sequoia scan with a data point every 1 ps closely matches the 10Hz scan (Fig. 3) showing the falling edge of the coherent pedestal and a prepulse at -14 ps.

We repeated this scan using the beam transmitted through the double PM system. The 50% transmission fraction was compensated by removing a neutral density filter so that the peak signal level was the same in both cases. We took shots either side of the peak to ensure our zero time was correct. With the PMs active the -30 ps and -90 ps prepulses are not reflected and the signal level remains below the Sequoia detection threshold (10^{-9}) until 2 ps before the peak of the pulse. We then measured in 200 fs steps to map out the rising edge of the cleaned pulse. We found that the intensity at -1.1 ps is $<10^{-6}$ of the peak intensity. At this point we had no free space remaining on the PM substrates so unfortunately do not know the temporal shape of the pulse between -1.1 ps and -100 fs.

Calculation of expected performance

Although we have found that the plasma mirrors work efficiently, eliminating prepulses and most of the coherent pedestal, the fact that their reflectivity turns on at -2 ps is not understood. The expected reflectivity of the two anti-reflection coated substrates is shown in Fig. 3. This is calculated using a measured reflectivity versus intensity dependence from Ref. 8 multiplied by the intensity measured in the 10 Hz contrast scan. For a peak intensity on the first plasma mirror of 10^{15} Wcm^{-2} , the ionization threshold of the glass is not reached until about 200 fs before the peak of the pulse. Activation of the plasma mirror at -2ps where the intensity is $\sim 10^{11} \text{ Wcm}^{-2}$ suggests a significant lowering of the ionization threshold. This is possibly caused by irradiation with several long prepulses and the several picosecond long coherent pedestal leading to plasma formation at a much earlier time [9]. It is interesting to note that a recent report on the characterization of a similar double PM system found the same switch on time of ~ 2 ps even though at that point their laser intensity was 10^5 of the peak intensity [10].

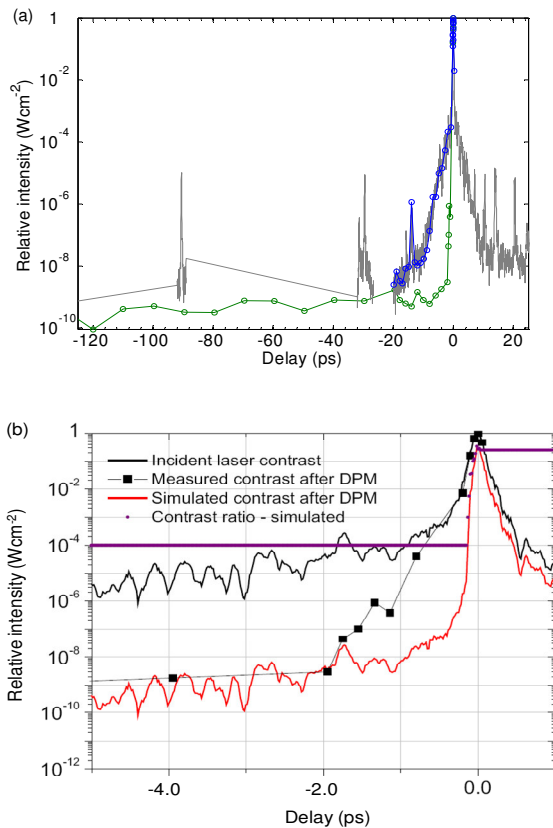


Figure 3. (a) Pulse contrast measured with the 10Hz beam (grey) and with full power shots (blue). The green data was measured after passage through the double plasma mirror system. (b) Detail of the rising edge of the pulse measured with the 10Hz beam (black solid) and after the plasma mirrors (black squares). The red line is a calculation of the expected contrast taking into account the intensity dependent reflectivity of the plasma mirrors.

Conclusions

We have characterized the Astra-Gemini double plasma mirror system in terms of the temporal contrast and measured the intensity at 1.1 ps before the main pulse to be at a level of 10^{-6} of the peak intensity. Further tests are necessary with different focusing conditions to optimize plasma mirror performance. The onset of substrate reflectivity is earlier than expected (-2 ps rather than -200 fs) which may indicate degradation of the optics through irradiation with low level prepulses.

References

1. B. Dromey et al., Phys. Rev. Lett. **99**, 085001 (2007).
2. D. Neely et al., Appl. Phys. Lett. **89**, 021502 (2006).
3. C. Hooker et al., this annual report.
4. C. Hooker et al., Opt. Express **19**, 2193 (2011).
5. N. V. Didenko et al., Opt. Express **16**, 3178 (2008).
6. M. J. V. Streeter et al., CLF Ann. Rep. 2008/2009, p.229
7. www.amplitude-technologies.com
8. Ch. Ziener et al., J. Appl. Phys. **93**, 768 (2003).
9. P. P. Rajeev et al., Phys. Rev. Lett. **102**, 083001 (2009).
10. A. Lévy et al., Opt. Lett. **32**, 310 (2007).

Fluka simulations of laser irradiated targets: thickness study for production of X-ray beams

Contact fxf817@bham.ac.uk

F. Fiorini

School of Physics and Astronomy, University of Birmingham,
Birmingham B15 2TT, UK

S. Green

Hall Edwards Radiotherapy Research Group, University Hospital
Birmingham NHS Trust, Birmingham B15 2TH, UK

R.J. Clarke, D. Neely

Central Laser Facility, STFC RAL, Oxfordshire OX11 0QX,
UK

Z. Najmudin

Physics Department, Imperial College London, London,
SW7 2AZ, UK

Introduction

During the interaction of the intense laser pulse with a target, a large part of the laser energy is converted into a population of hot electrons. The electron population is created on the target surface irradiated by the laser, with a spectrum believed to follow a relativistic Maxwellian distribution. Propagating inside the target they create a strong electric field, up to the order of TV/m. Given the very high current, their propagation requires a balancing return current from the background plasma. Upon reaching the rear surface of the target some of the hottest electrons escape, but most of them are attracted back into the target. A similar situation later occurs at the front of the target: most of the electrons return to the front surface and some escape. This phenomenon is called electron refluxing [1]. The percentage of refluxing electrons and the number of refluxes change with the target and laser beam characteristics [2, 3]. During its multiple paths inside the target, the electron beam emits X-rays, the characteristics of which are strictly dependent on the target and laser properties.

In this work we aim to show a simulation study of a simplified electron refluxing scheme in several different targets. Using theoretical hot electron spectra, the photon beams created in several targets have been investigated. Changing the target material and the thickness it was possible to obtain combinations giving the maximum photon yield as a function of the initial laser intensity.

Simulation implementation

At present, simulation programs capable of predicting exactly what happens in matter when a laser pulse hits a target are few. Some of them are not useable for all laser parameters and target thicknesses, and/or can only simulate some particular reactions. The simulations presented in this work have been performed using Fluka (FLUctuating KAskad) [4, 5], a Monte Carlo code for calculations of particle transport and interaction with matter. Given its aims, Fluka is not meant to simulate the reactions produced by lasers, but it can simulate the electron interactions producing the photon beam in cold matter. The reactions due to the electric field occurring in the target cannot be simulated using Fluka, so:

- 1) since the laser interacts with a very thin layer (few nanometers) of the target, the produced electron spectrum is only dependent on the laser characteristics and not on the target material;
- 2) the electron reflux is simulated by ‘hand’. The electron beam exiting the target is forced to re-enter the target: the spectrum of the outgoing electrons is saved and while 20% of the most energetic electrons can escape, 80% of them are forced to re-enter the target;
- 3) point 2) is repeated until the number of exiting electrons at the end of one of the reflux processes is null;

4) the spectra of the photons emitted forward at the end of each reflux process is saved and the sum of all the “forward” spectra is the result of this simulation study for each used target.

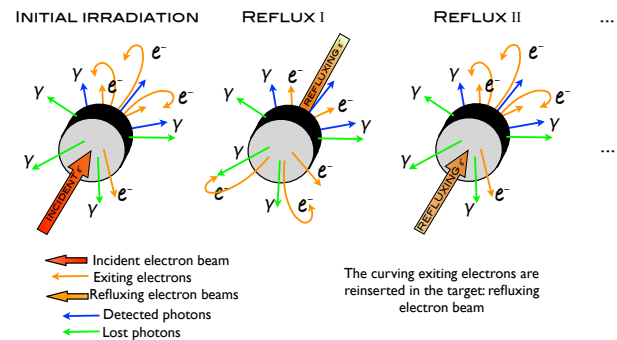


Fig.1 Simulation approach of the reflux process. The refluxing electrons, 80% of the exiting electrons with lower energy (curving orange arrows), are reinserted with their energy in the target as many times as needed to stop all of them in the target. The photon spectra are saved only for the photons emitted forward (blue arrows).

The initial electron spectrum follows a Maxwellian distribution where the temperature depends on the intensity and on the wavelength of the main laser pulse.

If the laser intensity is lower equal to 10^{19} Wcm^{-2} the $k_B T$ used is from Beg’s theory [6]:

$$k_B T \simeq 0.24 \left(\frac{I \lambda^2}{10^{18} \text{ Wcm}^{-2} \mu\text{m}^2} \right)^{1/3} \text{ MeV} \quad (1)$$

If the laser intensity is greater than 10^{19} Wcm^{-2} the $k_B T$ used is from Wilks’ theory [7]:

$$k_B T \simeq 0.511 \left(\sqrt{1 + \frac{I \lambda^2}{1.37 \times 10^{18} \text{ Wcm}^{-2} \mu\text{m}^2}} - 1 \right) \text{ MeV} \quad (2)$$

The beam propagates into the target without any initial divergence. In table 1 the used $k_B T$ values are shown in dependence on the laser intensity and in fig.2 the created initial electron spectra are illustrated. The wavelength used is the ASTRA GEMINI laser wavelength (0.8 μm).

Targets placed normally to the initial electron beam and made of different materials and with different thicknesses were simulated: Au, Ta, Cu, SiO_2 and PMMA. This wide selection was used to find out which material and which thickness maximises the number of produced X-rays and to compare the produced X-ray spectra.

GEMINI ($\lambda = 0.8 \mu\text{m}$)		
Laser Intensity (W/cm^2)	$k_B T$ (MeV)	Energy peak (MeV)
4.34×10^{17}	0.16	0.32
4.34×10^{18}	0.34	0.68
4.34×10^{19}	1.85	3.7
4.34×10^{20}	6.78	13.56
4.34×10^{21}	22.5	45

Table 1. The temperature ($k_B T$) and the peak energy of the Maxwellian spectrum of the simulated initial electrons are shown depending on the laser intensity.

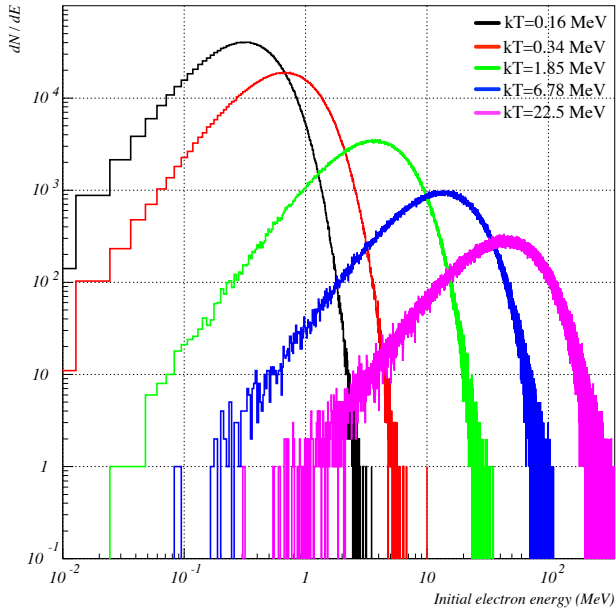


Fig.2 Initial electron spectrum for each studied value of $k_B T$. The total number of electrons is 2 millions in each spectrum.

Simulation results

Some of the photon spectra obtained are shown in fig.3. For reason of space we are not inserting the spectra obtained for each studied temperature and target thickness, but just some of

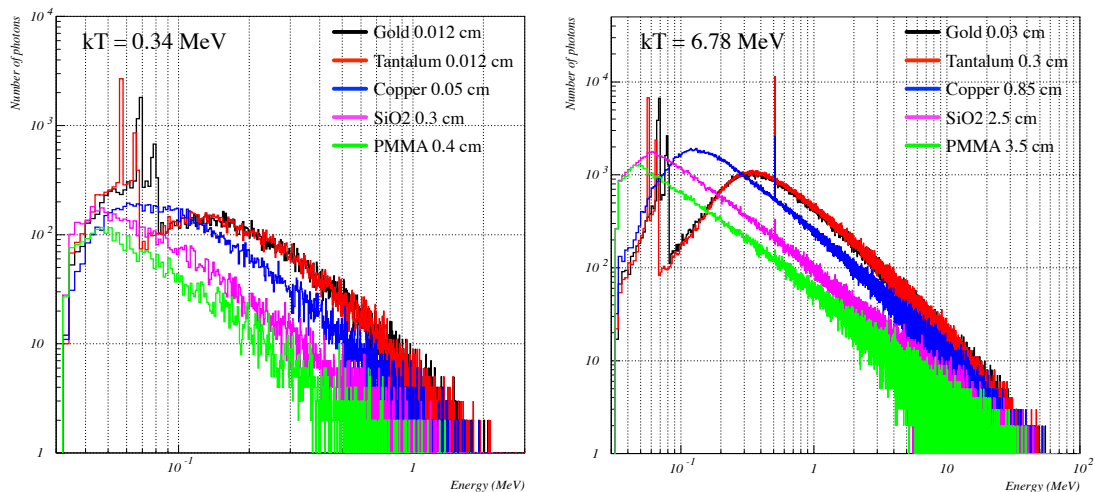


Fig. 3 Obtained spectra for $k_B T = 0.34$ (left) and $k_B T = 6.78$ MeV. The chosen thicknesses are those which maximise the number of forward emitted photons. The initial number of electrons was 3×10^5 for both the cases.

those obtained for $k_B T = 0.34$ and 6.78 MeV that according to the theory correspond to 4.34×10^{18} and $4.34 \times 10^{20} \text{ Wcm}^{-2}$.

Integrating the obtained spectra the total number of forward emitted photons can be found. The thicknesses of the targets shown in fig.3 are those which maximise the number of forward emitted photons for those initial electron spectra. The spectra giving the largest numbers of photons are always produced by the high Z materials (as expected from the bremsstrahlung effect) as well as the highest energy photons. The peak of the energy of the photons emitted from SiO_2 and PMMA targets is in both the cases below 100 keV and it does not greatly change its position with increasing initial electron energy even for the highest studied $k_B T$ (22.5 MeV). The tails in the spectra at high energies are always shorter for these materials than the tails created by the high Z targets (fact more noticeable in the case of $k_B T = 0.34$ MeV). The $K\alpha$ and $K\beta$ peaks are visible only for Au (energies between 66 and 80 keV) and Ta (energies between 55 and 67 keV) targets: this is because the energy threshold for particle transport in Fluka is 30 keV and the $K\alpha$ and $K\beta$ peaks for the other materials have energy lower than this threshold.

Running several simulations changing the thickness of the targets it was possible to determine the thickness maximising the photon yields. Fig. 4 shows the results of the simulations, where the photon yields are plotted as a function of the mass thickness.

Conclusions

In order to obtain the largest number of emitted photons, not only is the material important but also its thickness. Several applications can use laser generated X-ray beams and knowing the material and the thickness which maximise the yields or the ones giving a certain spectrum is always preferable.

The simulations discussed in this report still need to be fully benchmarked. A first experimental analysis is needed to understand the reliability of the theory giving the temperature of the laser accelerated electron beam. Unfortunately it is not possible to experimentally detect the primary accelerated electron beam, so its initial spectrum has to be determined from the spectrum of the electrons emitted from the target. Only then, we can do a more accurate comparison between the experimental data and the results obtained from these simplified simulations of the refluxing process.

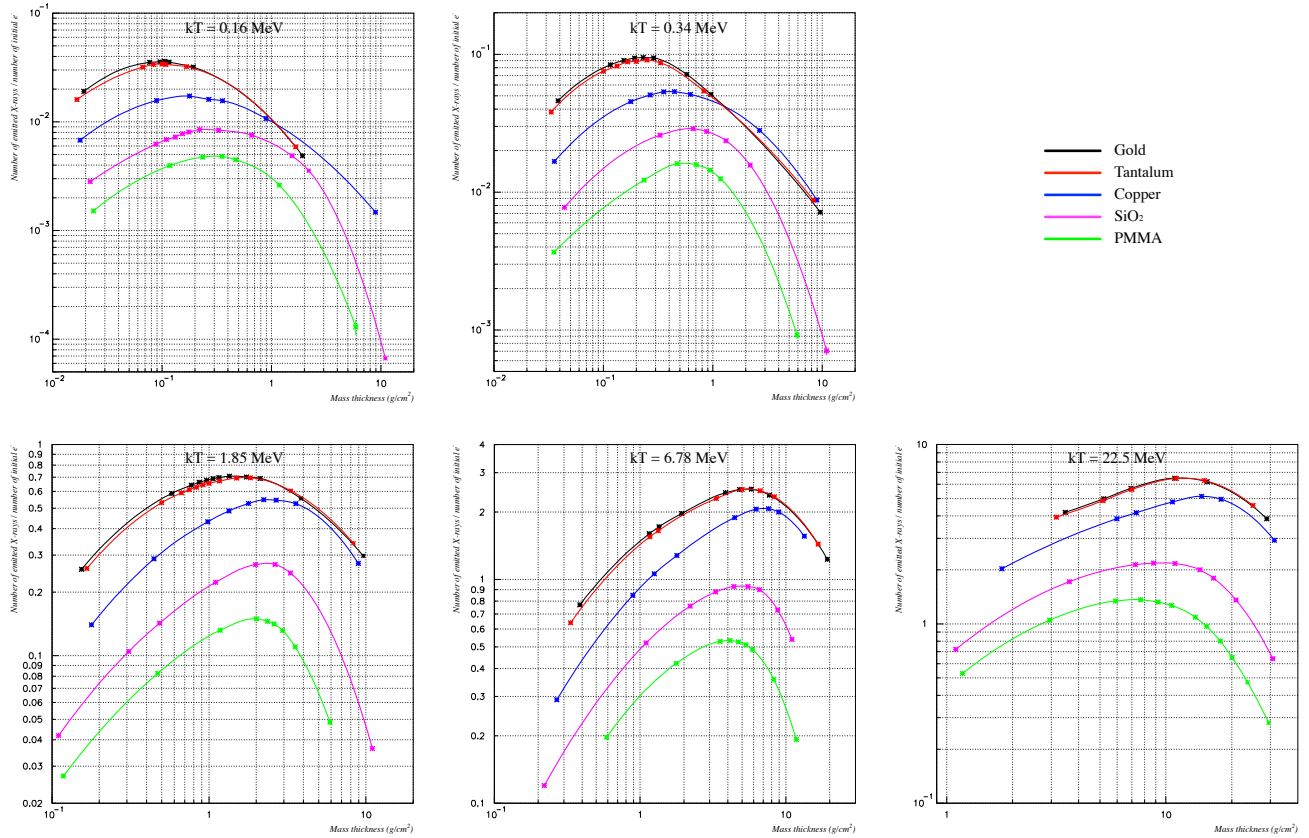


Fig. 4. Photon yields as a function of the target surface mass thickness for each studied temperature. The number of forward emitted photons is normalised by the number of initial electrons.

Acknowledgements

The work was funded by the LIBRA consortium grant from EPSRC, grant number EP/E035728/1.

References

1. AR Bell, JR Davies, S. Guerin, and H. Ruhl. *Fast-electron transport in high-intensity short-pulse laser-solid experiments*. Plasma physics and controlled fusion, 39:653, 1997.
2. J. Myatt, W. Theobald, JA Delettrez, C. Stoeckl, M. Storm, TC Sangster, AV Maximov, and RW Short. *High-intensity laser interactions with mass-limited solid targets and implications for fast-ignition experiments on OMEGA EP*. Physics of plasmas, 14:056301, 2007.
3. MN Quinn, XH Yuan, XX Lin, DC Carroll, O. Tresca, RJ Gray, M. Coury, C. Li, YT Li, CM Brenner, et al. *Refluxing of fast electrons in solid targets irradiated by intense, picosecond laser pulses*. Plasma Physics and Controlled Fusion, 53:025007, 2011.
4. G. Battistoni, S. Muraro, P.R. Sala, F. Cerutti, A. Ferrari, S. Roesler, A. Fasso', and J. Ranft. *The FLUKA code: Description and benchmarking*. Proceedings of the Hadronic Shower Simulation Workshop 2006, Fermilab 6–8 September 2006, M. Albrow, R. Raja eds., AIP Conference Proceeding, 896:31–49, 2007.
5. A. Fasso', A. Ferrari, J. Ranft, and P.R. Sala. *FLUKA: a multi-particle transport code*, CERN-2005-10. INFN/TC 05/11, SLAC-R-773, 2005.
6. F. N. Beg, A. R. Bell, A. E. Dangor, C. N. Danson, A. P. Fews, M. E. Glinsky, B. A. Hammel, P. Lee, P. A. Norreys, and M. Tatarakis, *A study of picosecond laser–solid interactions up to 10^{19} Wcm⁻²*, Phys. Plasmas 4 (2), 447, 1997.
7. SC Wilks, AB Langdon, TE Cowan, M. Roth, M. Singh, S. Hatchett, MH Key, D. Pennington, A. MacKinnon, and RA Snavely. *Energetic proton generation in ultra-intense laser–solid interactions*. Physics of Plasmas, 8:542, 2001.